Universiteit Leiden
The Netherlands

# The H2CO abundance in the inner warm regions of low-mass protostellar envelopes

Maret, S.; Ceccarelli, C.; Caux, E.; Jørgensen, J.K.; Dishoeck, E.F. van; Tielens, A.G.G.M.

**Citation**
Maret, S., Ceccarelli, C., Caux, E., Jørgensen, J. K., Dishoeck, E. F. van, & Tielens, A. G. G. M. (2004). The H2CO abundance in the inner warm regions of low-mass protostellar envelopes. *Astron. Astrophys.*, *416*, 577-594. Retrieved from https://hdl.handle.net/1887/2201

Version: Not Applicable (or Unknown)
License:
Downloaded from: https://hdl.handle.net/1887/2201

**Note:** To cite this publication please use the final published version (if applicable).

A&A 416, 577–594 (2004)
DOI: 10.1051/0004-6361:20034157
© ESO 2004

Astronomy & Astrophysics

# The $H_2CO$ abundance in the inner warm regions of low mass protostellar envelopes⋆

S. Maret[1], C. Ceccarelli[2], E. Caux[1], A. G. G. M. Tielens[3], J. K. Jørgensen[4], E. van Dishoeck[4], A. Bacmann[5], A. Castets[6], B. Lefloch[2], L. Loinard[7], B. Parise[1], and F. L. Schöier[4]

[1] Centre d'Étude Spatiale des Rayonnements, CESR/CNRS-UPS, BP 4346, 31028 Toulouse Cedex 04, France
[2] Laboratoire d'Astrophysique, Observatoire de Grenoble, BP 53, 38041 Grenoble Cedex 09, France
[3] Space Research Organization of the Netherlands, PO Box 800, 9700 AV Groningen, The Netherlands
[4] Leiden Observatory, PO Box 9513, 2300 RA Leiden, The Netherlands
[5] European Southern Observatory, Karl-Schwarzschild Str. 2, 85748 Garching bei München, Germany
[6] Observatoire de Bordeaux, BP 89, 33270 Floirac, France
[7] Instituto de Astronomía, Universidad Nacional Autónoma de México, Apartado Postal 72-3 (Xangari), 58089 Morelia, Michoacán, Mexico

Received 4 August 2003 / Accepted 9 October 2003

**Abstract.** We present a survey of the formaldehyde emission in a sample of eight Class 0 protostars obtained with the IRAM and JCMT millimeter telescopes. The range of energies of the observed transitions allows us to probe the physical and chemical conditions across the protostellar envelopes. The data have been analyzed with three different methods with increasing level of sophistication. We first analyze the observed emission in the LTE approximation, and derive rotational temperatures between 11 and 40 K, and column densities between 1 and $20 \times 10^{13}$ cm$^{-2}$. Second, we use a LVG code and derive higher kinetic temperatures, between 30 and 90 K, consistent with subthermally populated levels and densities from 1 to $6 \times 10^5$ cm$^{-3}$. The column densities from the LVG modeling are within a factor of 10 with respect to those derived in the LTE approximation. Finally, we analyze the observations based upon detailed models for the envelopes surrounding the protostars, using temperature and density profiles previously derived from continuum observations. We approximate the formaldehyde abundance across the envelope with a jump function, the jump occurring when the dust temperature reaches 100 K, the evaporation temperature of the grain mantles. The observed formaldehyde emission is well reproduced only if there is a jump of more than two orders of magnitude, in four sources. In the remaining four sources the data are consistent with a formaldehyde abundance jump, but the evidence is more marginal ($\leq 2\ \sigma$). The inferred inner $H_2CO$ abundance varies between $1 \times 10^{-8}$ and $6 \times 10^{-6}$. The absolute values of the jump in the $H_2CO$ abundance are uncertain by about one order of magnitude, because of the uncertainties in the density, ortho to para ratio, temperature and velocity profiles of the inner region, as well as the evaporation temperature of the ices. We discuss the implications of these jumps for our understanding of the origin and evolution of ices in low mass star forming regions. Finally, we give predictions for the submillimeter $H_2CO$ lines, which are particularly sensitive to the abundance jumps.

**Key words.** ISM: abundances – ISM: molecules – stars: formation – ISM: general

## 1. Introduction

Low mass protostars form from dense fragments of molecular clouds. During the pre-collapse and collapse phases, the physical and chemical composition of the matter undergoes substantial, sometimes spectacular, changes. From a chemical point of view, the pre-collapse phase is marked by the freezing of molecules onto the grain mantles. In the very inner parts of the pre-stellar condensations, molecules have been observed to progressively disappear from the gas phase (e.g. Tafalla et al. 2002; Bergin et al. 2002). The CO molecule, whose condensation temperature is around 20 K, is the best studied species both because it is the most abundant molecule after $H_2$, and because of its important role in the gas thermal cooling. CO depletion of more than a factor of ten has been observed in the centers of these condensations (Caselli et al. 1998, 2002; Bacmann et al. 2002). This large CO depletion is accompanied by a variety of changes in the molecular composition; the most spectacular is the dramatic increase in the molecular deuteration (up to eight orders of magnitude with respect to the D/H elemental abundance) observed in formaldehyde (Bacmann et al. 2003). The changes are recorded in the grain mantles, where the pre-collapse gas will be progressively stored. When a protostar is finally born, the dust cocoon warms

*Send offprint requests to*: S. Maret,
e-mail: sebastien.maret@obs.ujf-grenoble.fr

⋆ Appendices A and B are only available in electronic form at http://www.edpsciences.org

up and the mantle species evaporate into the gas phase, returning information from the previous phase.

Most of the studies of the composition of the grain mantles have been so far carried out towards massive protostars, because they have strong enough IR continua against which the absorption of ices can be observed (e.g. Gerakines et al. 1999; Dartois et al. 1999; Gibb et al. 2000). The absorption technique allows one to detect the most important constituents of the grain mantles: $H_2O$, CO, $CO_2$, and sometime $NH_3$, $CH_3OH$ and $H_2CO$ (Schutte et al. 1996; Keane et al. 2001). In much cases, the mantle composition of low mass protostars has been directly observed. In these cases, the observations have been carried out towards protostars that possess a strong enough IR continuum (e.g. Boogert et al. 2000b). If our understanding of the evolution of a protostar is basically correct, those protostars, typically Class I or border line Class II sources, represent a relatively evolved stage, where most of the original envelope has already been dispersed (e.g. Shu et al. 1987; André et al. 2000). Furthermore, the observed absorption may be dominated by foreground molecular clouds (Boogert et al. 2002). Thus, direct observations of the chemical composition of the primeval dust mantles of low mass protostars have so far proven to be elusive.

Alternatively, one can carry out an "archeological" study, looking at the composition of the gas in the regions, which are known or suspected to be dominated by the gas desorbed from grain mantles. This technique has the advantage of being much more sensitive than the absorption technique, as it can detect molecules whose abundance (with respect to $H_2$) is as low as $\sim 10^{-11}$ against a limit of $\sim 10^{-6}$–$10^{-7}$ reachable with the absorption technique. Indeed, several very complex molecules observed in the warm ($\geq$100 K) gas of the so called *hot cores* have been considered hallmarks of grain mantle evaporation products (e.g. Blake et al. 1987). Once in the gas phase, molecules like formaldehyde and methanol, initially in the grain mantles, trigger the formation of more complex molecules, referred to as daughter or second-generation molecules (e.g. Charnley et al. 1992; Caselli et al. 1993). The gas temperature and density are other key parameters in the chemical evolution of the gas, which has the imprint of the precollapse phase.

So far, hot cores have been observed in massive protostars, and are believed to represent the earliest stages of massive star formation, when the gas is not yet ionized by the new born star (Kurtz et al. 2000). Recently, however, it has been proposed that low mass protostars might also harbor such hot cores. Note that the definition of hot core is not unanimous in the literature. Here we mean a region where the chemical composition reflects the evaporation of the ice mantles and subsequent reactions between those species (e.g. Rodgers & Charnley 2003). In this respect, Ceccarelli et al. (2000a,c) claimed that the low mass protostar IRAS 16293-2422 shows evidence of an inner region (~400 AU in size) warm enough ($\geq$100 K) to evaporate the grain mantles, a claim substantially confirmed by Schöier et al. (2002). Indeed, very recent observations by Cazaux et al. (2003; see also Ceccarelli et al. 2000b) reveal also the presence of organic acids and nitriles in the core of IRAS 16293-2422, substantiating the thesis of a hot core region in which not only the ices have evaporated but also a subsequent hot core chemistry has ensued. Furthermore, Maret et al. (2002) argued that NGC 1333-IRAS 4, another low mass very embedded protostar, has also such a warm region, somewhat less than 200 AU in size.

Formaldehyde is a relatively abundant constituent of the grain mantles and it is a basic organic molecule that forms more complex molecules (e.g. Charnley et al. 1992). For this reason, we studied the formaldehyde line emission originating in the envelopes of a sample of very embedded, Class 0 low mass protostars. In this article we report the first results of this systematic study. This is part of a larger project aimed to characterize as far as possible the physical and chemical composition of low mass protostars during the first phases of formation. Jørgensen et al. (2002) determined the temperature and density structure for these sources and the CO abundance in the outer regions. A forthcoming paper will address the methanol line emission in the same source sample, as methanol is another key organic mantle constituent, linked by a common formation route with formaldehyde.

One of the ultimate goals of the present study is to understand the efficiency of $H_2CO$ against $CH_3OH$ formation in low mass protostars, whether and how it depends on the parental cloud, and to compare it with the case of massive protostars. An immediate goal of the present article is to study the formaldehyde abundance profile in the surveyed sample of low mass protostars. In a previous study that we carried out towards IRAS 16293-2422, we concluded that formaldehyde forms on grain mantles and is trapped mostly in $H_2O$-rich ices in the innermost regions of the envelope and mostly in CO-rich ices in the outermost regions (Ceccarelli et al. 2000c, 2001). As the dust gradually warms up going inwards, formaldehyde is released from the icy mantles all along the envelope. In the hot core like region ($r \leq 200$ AU) the formaldehyde abundance jumps by about a factor 100 to $\sim 1 \times 10^{-7}$ (Ceccarelli et al. 2000c; Schöier et al. 2002). Similarly, formaldehyde enhancement is observed in several outflows, because of ice mantle sputtering in shocks (Bachiller & Perez Gutierrez 1997; Tafalla et al. 2000). In contrast, no jump of formaldehyde abundance has been detected in the sample of massive protostars studied by van der Tak et al. (2000). To firmly assess whether and by how much formaldehyde is systematically more abundant in the interiors of low compared to high mass protostars, a survey of more low mass protostars has to be carried out. This will allow us to answer some basic questions such as how, when and how much formaldehyde is formed on the grain mantles. Given that it forms more complex molecules (e.g. Bernstein et al. 1999) knowing the exact abundance of formaldehyde is fundamental to answer the question of whether or not pre- and/or biotic molecules can be formed in the 200 or so inner AUs close to the forming star.

In this article we report observations of formaldehyde emission in a sample of eight Class 0 sources. After a preliminary analysis (rotational diagrams and LVG analysis), the observations are analyzed in terms of an accurate model that accounts for the temperature and density gradients in each source, as well as the radiative transfer, which includes FIR photon pumping of the formaldehyde levels. The article is organized as

**Table 1.** The observed sample. IRAS16293-2422, which has been studied elsewhere (see text) is included for comparison.

| Source | $\alpha$(2000) | $\delta$(2000) | Cloud | Dist.[a] (pc) | $L_{bol}$[b] ($L_\odot$) | $M_{env}$[b] ($M_\odot$) | $L_{smm}/L_{bol}$[c] (%) | $T_{bol}$[b] (K) |
|---|---|---|---|---|---|---|---|---|
| NGC 1333-IRAS 4A | 03:29:10.3 | +31:13:31 | Perseus | 220 | 6 | 2.3 | 5 | 34 |
| NGC 1333-IRAS 4B | 03:29:12.0 | +31:13:09 | Perseus | 220 | 6 | 2.0 | 3 | 36 |
| NGC 1333-IRAS 2 | 03:28:55.4 | +31:14:35 | Perseus | 220 | 16 | 1.7 | $\lesssim$1 | 50 |
| L1448-MM | 03:25:38.8 | +30:44:05 | Perseus | 220 | 5 | 0.9 | 2 | 60 |
| L1448-N | 03:25:36.3 | +30:45:15 | Perseus | 220 | 6 | 3.5 | 3 | 55 |
| L1157-MM | 20:39:06.2 | +68:02:22 | Isolated | 325 | 11 | 1.6 | 5 | 60 |
| L1527 | 04:39:53.9 | +26:03:10 | Taurus | 140 | 2 | 0.9 | 0.7 | 60 |
| VLA1623 | 16:26:26.4 | –24:24:30 | $\rho$-Ophiuchus | 160 | 1 | 0.2 | 10 | <35 |
| IRAS 16293-2422[d] | 16:32:22.7 | –24:38:32 | $\rho$-Ophiuchus | 160 | 27 | 5.4 | 2 | 43 |

[a] From André et al. (2000), except for Perseus sources (Cernis 1990).
[b] From Jørgensen et al. (2002).
[c] From André et al. (2000).
[d] Included for comparison.

follows: we first explain the criteria that lead to the source and line selection and the observations carried out (Sect. 2). In Sect. 3 we describe the results of the observations, in Sect. 4 we derive the approximate gas temperature, density and $H_2CO$ column density of each source by means of the standard rotational diagram technique and by a non-LTE LVG model. In Sect. 5 we derive the formaldehyde abundance in the inner and outer parts of the envelope of each source, with an accurate model that takes into account the structure of the protostellar envelopes. Finally, in Sect. 6 we discuss the implications of our findings, and conclude in Sect. 7.

## 2. Observations

### 2.1. Target and line selection

We observed a sample of eight protostars, all of them *Class 0* sources (André et al. 2000) located in the Perseus, $\rho$-Ophiuchus and Taurus complexes, except L1157-MM that lies in an isolated clump (Bachiller & Perez Gutierrez 1997). The eight selected sources are among the brightest Class 0 sources in the André et al. (2000) sample. Their physical structure (dust density and temperature profiles) has been determined from their continuum emission by Jørgensen et al. (2002) except for L1448-N, which is analyzed in this paper (see Appendix A).

The source distances quoted by Jørgensen et al. (2002) were adopted. The list of the selected sources is reported in Table 1 together with their bolometric luminosity, envelope mass, the ratio of the submillimeter to bolometric luminosity, and the bolometric temperature and distance. In the same table, we also report the data relative to IRAS 16293-2422, which was previously observed in $H_2CO$ transitions by van Dishoeck et al. (1995) and Loinard et al. (2000), and studied in Ceccarelli et al. (2000c) and Schöier et al. (2002). IRAS 16293-2422 will be compared to the other sources of the sample.

A list of eight transitions was selected, three ortho-$H_2CO$ transitions and five para-$H_2CO$ transitions (Table 2). When possible, the corresponding isotopic lines were observed in order to derive the line opacity. The transitions were selected to cover a large range of upper level energies (between ~20 and ~250 K) with relatively large spontaneous emission coefficients $A_{u,l}$ ($\geq 10^{-4}$ s$^{-1}$). The latter condition is dictated by the necessity to detect the line, whereas the first condition aims to obtain lines that probe different regions of the envelope. Finally, practical considerations, namely having more than one line in a single detector setting, provided a further constraint. In the final selection we were helped by our pilot study on IRAS 16293-2422 (Ceccarelli et al. 2000c) and by previous studies of the formaldehyde emission in molecular clouds and protostellar envelopes (Mangum & Wootten 1993; Jansen et al. 1994, 1995; Ceccarelli et al. 2003).

The formaldehyde transitions between 140 and 280 GHz were observed with the single dish IRAM-30 m telescope[1], located at the summit of Pico Veleta in Spain. Higher frequency lines were observed at the JCMT[2], a 15 m single dish telescope located at the summit of Mauna Kea, Hawaii. The choice of the two telescopes allows us to have roughly similar beam sizes over the observed frequencies.

### 2.2. IRAM observations

The IRAM observations were carried out in November 1999[3] and September 2002. The various receivers available at the 30 m were used in different combinations to observe at least four transitions simultaneously. The image sideband rejection was always higher than 10 dB, and typical system temperatures

[1] IRAM is an international venture supported by INSU/CNRS (France), MPG (Germany) and IGN (Spain).

[2] The JCMT is operated by the Joint Astronomy Center in Hilo, Hawaii on behalf of the present organizations: The Particle Physics and Astronomy Research Council in the UK, the National Research Council of Canada and the Netherlands Organization for Scientific Research.

[3] IRAM November 1999 data have also been presented in Loinard et al. (2002a).

**Table 2.** Integrated fluxes of $H_2CO$ lines in $T_{mb}\,dV$ units. Upper limits are given as 2 $\sigma$. The "-" symbol indicates lack of the relevant observation.

| | o-$H_2CO$ | | | p-$H_2CO$ | | | | |
|---|---|---|---|---|---|---|---|---|
| Transition | $2_{1,2}$–$1_{1,1}$ | $4_{1,4}$–$3_{1,3}$ | $5_{1,5}$–$4_{1,4}$ | $3_{0,3}$–$2_{0,2}$ | $3_{2,2}$–$2_{2,1}$ | $5_{0,5}$–$4_{0,4}$ | $5_{2,4}$–$4_{2,3}$ | $5_{4,2}$–$4_{4,1}$[a] |
| $E_u$ (K) | 21.9 | 45.6 | 62.4 | 21.0 | 68.1 | 52.2 | 96.7 | 234 |
| $A_{u,l}$ ($s^{-1}$) | $5.4 \times 10^{-5}$ | $6.0 \times 10^{-4}$ | $1.2 \times 10^{-3}$ | $2.9 \times 10^{-4}$ | $1.6 \times 10^{-4}$ | $1.4 \times 10^{-3}$ | $1.2 \times 10^{-3}$ | $5.0 \times 10^{-4}$ |
| $\nu$ (GHz) | 140.839 | 281.527 | 351.769 | 218.222 | 218.476 | 362.736 | 363.946 | 364.103 |
| $g_u$ | 5 | 9 | 11 | 7 | 7 | 11 | 11 | 11 |
| Telescope | IRAM | IRAM | JCMT | IRAM | IRAM | JCMT | JCMT | JCMT |
| HPBW (") | 17 | 9 | 14 | 11 | 11 | 14 | 14 | 14 |
| $\eta_{mb}$ or $B_{eff}/F_{eff}$ | 0.74 | 0.47 | 0.63 | 0.62 | 0.62 | 0.63 | 0.63 | 0.63 |
| NGC 1333-IRAS 4A | 9.1 ± 1.4 | 10.6 ± 2.6 | 5.5 ± 1.2 | 9.3 ± 1.9 | 2.2 ± 0.4 | 2.9 ± 1.0 | 1.2 ± 0.6 | 1.7 ± 0.9 |
| NGC 1333-IRAS 4B | 6.8 ± 1.0 | 12.1 ± 3.0 | 7.5 ± 1.7 | 9.6 ± 1.9 | 4.7 ± 1.0 | 5.9 ± 2.1 | 3.6 ± 1.0 | 0.9 ± 0.6 |
| NGC 1333-IRAS 2 | 4.3 ± 0.6 | 5.8 ± 1.5 | 1.6 ± 0.4 | 4.9 ± 1.0 | 1.0 ± 0.2 | 1.8 ± 0.6 | 0.6 ± 0.4 | <0.4 |
| L1448-MM | 3.3 ± 0.7 | 4.7 ± 1.1 | 1.0 ± 0.2 | 3.4 ± 0.6 | 0.4 ± 0.1 | 1.3 ± 0.4 | 0.2 ± 0.1 | <0.1 |
| L1448-N | 7.9 ± 0.9 | 6.9 ± 1.6 | 3.8 ± 0.9 | 5.7 ± 0.9 | - | - | 0.6 ± 0.2 | - |
| L1157-MM | 1.2 ± 0.2 | 2.1 ± 0.5 | 1.2 ± 0.3 | 1.1 ± 0.3 | <0.2 | 0.5 ± 0.2 | <0.1 | <0.1 |
| L1527 | 2.8 ± 0.7 | 4.5 ± 1.1 | 1.0 ± 0.3 | 3.0 ± 1.3 | 0.2 ± 0.1 | 0.4 ± 0.2 | - | - |
| VLA1623 | 3.8 ± 1.2 | 2.7 ± 1.2 | 0.9 ± 0.2 | 5.0 ± 1.5 | - | 1.2 ± 0.4 | <0.2 | <0.3 |

[a] Blended with the $5_{4,1}$–$4_{4,0}$ $H_2CO$ line.

were 200−300 K at 2 mm, and 200−500 K at 1 mm. The intensities reported in this paper are expressed in main beam temperature units, given by:

$$T_{mb} = \frac{F_{eff}}{B_{eff}} T_A^* \quad (1)$$

where $B_{eff}$ is the main beam efficiency, and $F_{eff}$ is the forward efficiency. The main beam efficiency is 69%, 57% and 42% at 140, 220 and 280 GHz respectively, and the forward efficiency is 93%, 91% and 88% at the same frequencies. Each receiver was connected to an autocorrelator unit. For the 1 and 2 mm bands, a spectral resolution of 80 kHz and a bandwidth of 80 MHz was used. These spectral resolutions correspond to a velocity resolution of 0.09−0.17 km $s^{-1}$ depending on frequency. All IRAM observations were obtained in position switching mode. The absolute calibration was regularly checked and was about 10%, 15% and 20% at 140−170 GHz, 220−240 GHz and 280 GHz respectively. Pointing was also regularly checked and was better than 3″.

### 2.3. JCMT observations

The JCMT observations were obtained in February 2001, August 2001 and February 2002. The single sideband dual polarization receiver B3 was used with the Digital Autocorrelation Spectrometer (DAS). Typical system temperatures were 400 to 800 K. A spectral resolution of 95 kHz for a 125 MHz bandwidth was used for most of the lines, while a resolution of 378 kHz for a bandwidth of 500 MHz was used to observe some of the lines simultaneously. These spectral resolutions correspond to a velocity resolution of 0.08−0.32 km $s^{-1}$. The antenna temperatures were converted into main beam temperature scale using[4]

$$T_{mb} = \frac{T_A^*}{\eta_{mb}} \quad (2)$$

where $\eta_{mb}$ is the main beam efficiency, equal to 63% at the observed frequencies. The calibration and pointing were regularly checked using planets and were found to be better than 30% and 3″ respectively. The JCMT observations were obtained in beam switching mode, with a 180″ offset.

## 3. Results

The observed $H_2CO$ line spectra are shown in Figs. 1 and 2 and the results of the observations are summarized in Table 2.

Most of the lines are relatively narrow ($FWHM \sim$ 2−3 km $s^{-1}$) with a small contribution (≤5%) from wings extending to larger velocities. The higher the upper level energy of the transition the lower the contribution of the wings, which practically disappear in the lines observed with JCMT. NGC 1333-IRAS 4A and NGC 1333-IRAS 4B represent an exception to this picture. The line spectra of these two sources are broad (∼5 km $s^{-1}$) and the wings are more pronounced than in the other sources. Evidence of self-absorption and/or absorption from foreground material is seen in most sources, in particular in low lying lines.

In this study we focus on the emission from the envelopes surrounding the protostars. Hence, we are interested in the intensity of the narrow component of the lines, that we fitted with

[4] JCMT does not follow the same convention for antenna temperature than IRAM, the JCMT antenna temperature $T_A^*$ being already corrected for the forward efficiency of the antenna.

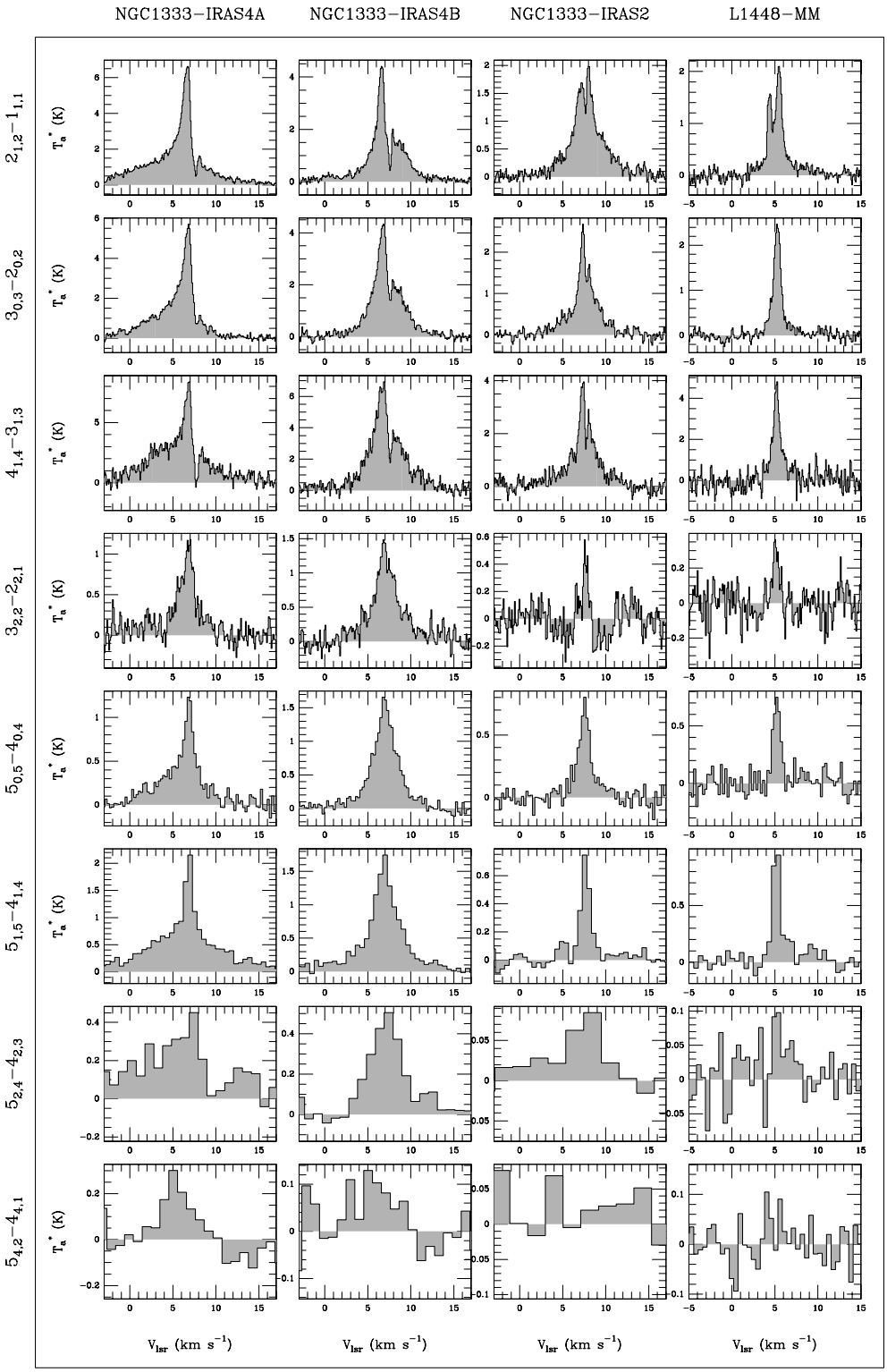


**Fig. 1.** Spectra of the eigth $H_2CO$ transitions in Table 2 observed towards NGC 1333-IRAS 4A, NGC 1333-IRAS 4B, NGC 1333-IRAS 2, and L1448-MM respectively.

a Gaussian. In some cases, a residual due to the "high" velocity wings remains, and that has not been included in the line flux estimate. When a Gaussian fitting was not possible because of self-absorption, the flux of the lines was estimated by integrating over a velocity range of ±2 km s$^{-1}$ around the source $V_{\rm lsr}$. This velocity range corresponds to the width of the lines with high upper level energies, where self-absorption is less important. For these lines, the self-absorption is included in the line flux determination, and the flux measured is therefore slightly smaller than the one that would have been obtained by a Gaussian fitting. We observed the brightest lines in the $^{13}$C isotopomer of formaldehyde, as reported in Table 3.

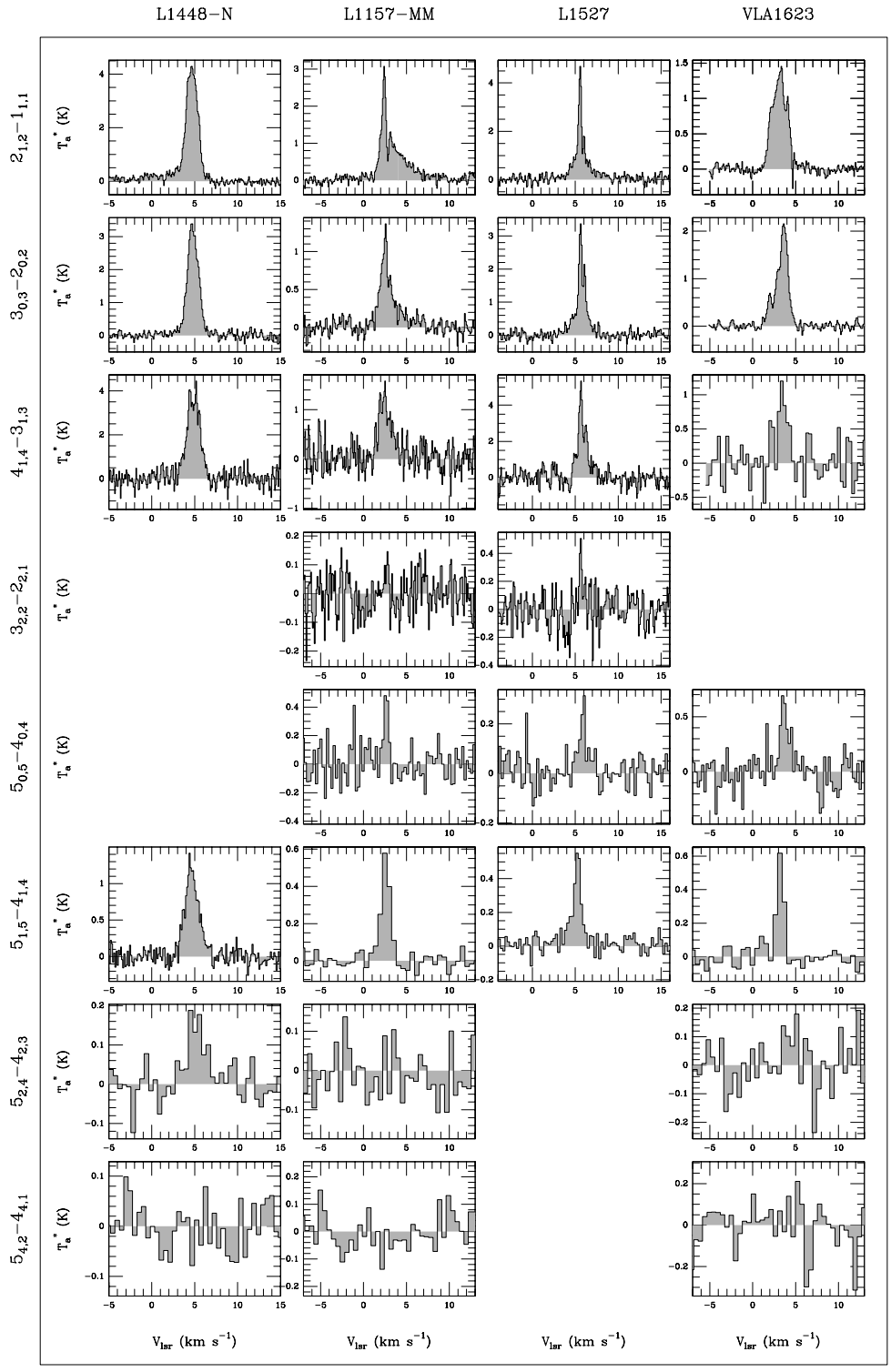


**Fig. 2.** As Fig. 1 for the sources L1448-N, L1157-MM, L1527 and VLA1623.

Finally, the errors quoted in Tables 2 and 3 include both the statistical uncertainties and the calibration error. For non detected lines we give the $2\sigma$ upper limit defined as follows:

$$F_{\rm max} = 2(1+\alpha)\,\sigma\,\sqrt{\Delta v\,\delta v} \quad (3)$$

where $\sigma$ is the rms per channel, $\Delta v$ is the line width estimated from detected lines on the same source, $\delta v$ is the channel width, and $\alpha$ is the calibration uncertainty.

## 4. Approximate analysis

### 4.1. Line opacities

The detection of some $H_2^{13}CO$ transitions allows to estimate the line opacities of the relevant $H_2^{12}CO$ lines. Using the escape probability formalism and assuming that the $H_2^{13}CO$ lines are

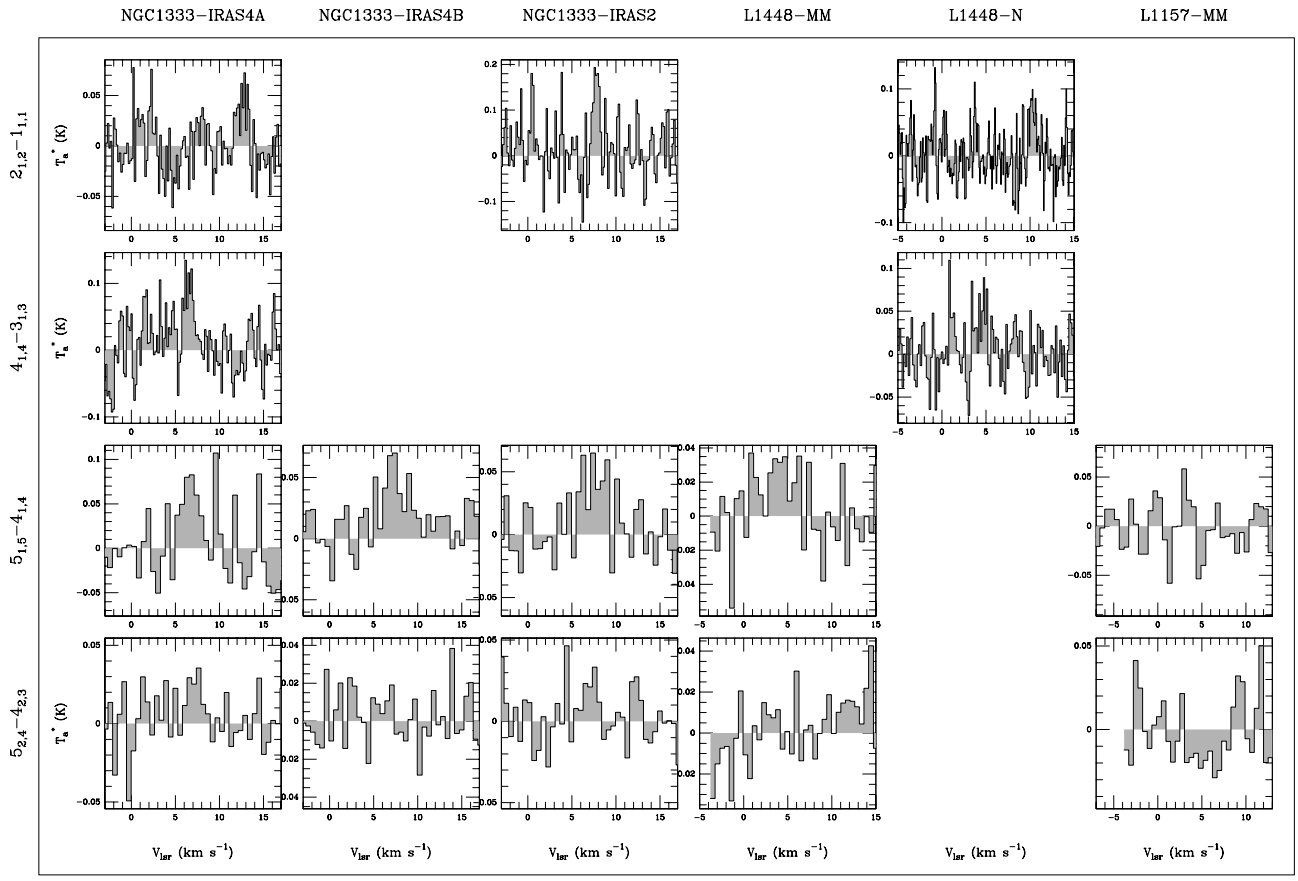


**Fig. 3.** Spectra of the observed $H_2^{13}CO$ lines.

optically thin, the ratio between the $H_2^{13}CO$ and $H_2^{12}CO$ line fluxes can be expressed as:

$$\frac{F_{H_2^{12}CO}}{F_{H_2^{13}CO}} = \frac{\left[^{12}C\right]}{\left[^{13}C\right]}\beta \quad (4)$$

where $\beta$ is the escape probability, which, in the case of a homogeneous slab of gas (de Jong et al. 1980), is equal to:

$$\beta = \frac{1 - \exp(-3\tau)}{3\tau} \quad (5)$$

and $\frac{[^{12}C]}{[^{13}C]}$ is the isotopic elemental ratio, equal to 70 (Boogert et al. 2000a). In the previous equation, we assume that the $H_2^{12}CO$ to $H_2^{13}CO$ ratio is equal to the isotopic elemental ratio, as supported by the available observations (e.g. Schöier et al. 2002). Using this equation, the opacities values reported in Table 4 are obtained.

The opacity values reported in Table 4 are relatively low, which indicates that the lines are moderately thick, vwith the exception of the line at 351 GHz towards NGC 1333-IRAS 2. The uncertainty on the latter opacity is however relatively large, as shown by the errors bars reported in Table 4.

### 4.2. Rotational diagram analysis

To obtain a first order estimate, we derived the beam-averaged column density of formaldehyde and rotational temperature by means of the standard rotational diagram technique (see Goldsmith & Langer 1999 for a general description of the method, and Mangum & Wootten 1993 for its application to formaldehyde lines).

Figure 4 shows the $H_2CO$ rotational diagrams of the observed sources. In these diagrams, the ortho to para ratio of formaldehyde was kept as a free parameter, and was derived by minimizing the $\chi^2$ between the observed fluxes and the rotational diagram predictions. The best agreement is obtained for a value of about 2 on all the sources. The fact that this value is lower than the high-temperature limit of 3 suggest that the formaldehyde is formed at low temperature, around 20 K (Kahane et al. 1984). However, while this ratio seems to be the same for all sources, we emphasize that it is highly uncertain. In particular, the fact that the same transitions have been observed on all the sources can lead to systematic errors on this value. A more accurate derivation of the ortho to para ratio would need a correction for the line opacities, which has the effect of scattering the points in the rotational diagram (see Goldsmith & Langer 1999, for a review on the effect of opacities in a rotational diagram). This correction is not possible here as only a limited number of $H_2^{13}CO$ transitions has been observed. The $5_{2,4}$–$4_{2,3}$ line was only detected towards NGC 1333-IRAS 4A and NGC 1333-IRAS 4B. Because of its high energy (234 K), this line is probably excited in hotter regions, and would increase the derived rotational temperature. This line was not included to keep the derived parameters comparable from one source to the other.

**Table 3.** Integrated fluxes of $H_2{}^{13}CO$ lines in $T_{mb}\,dV$ units. Upper limits are given as 2 $\sigma$. The "-" symbol indicates lack of the relevant observation.

| | o-$H_2^{13}CO$ | | | p-$H_2^{13}CO$ |
|---|---|---|---|---|
| Transition | $2_{1,2}$–$1_{1,1}$ | $4_{1,4}$–$3_{1,3}$ | $5_{1,5}$–$4_{1,4}$ | $5_{2,4}$–$4_{2,3}$ |
| $E_u$ (K) | 21.7 | 44.8 | 61.3 | 98.5 |
| $A_{u,l}$ ($s^{-1}$) | $1.5 \times 10^{-4}$ | $1.7 \times 10^{-3}$ | $3.4 \times 10^{-3}$ | $1.1 \times 10^{-3}$ |
| $\nu$ (GHz) | 137.450 | 274.762 | 343.325 | 354.899 |
| HPBW ($''$) | 17 | 9 | 14 | 14 |
| Telescope | IRAM | IRAM | JCMT | JCMT |
| $\eta_{mb}$ or $B_{eff}/F_{eff}$ | 0.74 | 0.47 | 0.63 | 0.63 |
| NGC 1333-IRAS 4A | 0.4 ± 0.1 | 0.3 ± 0.1 | 0.3 ± 0.2 | <0.1 |
| NGC 1333-IRAS 4B | - | - | 0.3 ± 0.1 | <0.1 |
| NGC 1333-IRAS 2 | 0.2 ± 0.1 | - | 0.4 ± 0.2 | <0.1 |
| L1448-MM | - | - | <0.1 | <0.2 |
| L1448-N | 0.2 ± 0.1 | <0.1 | - | - |
| L1157-MM | - | - | <0.1 | <0.1 |

**Table 4.** $H_2CO$ lines opacities derived from the $H_2{}^{13}CO$ observations.

| | o-$H_2CO$ | | | p-$H_2CO$ |
|---|---|---|---|---|
| Transition | $2_{1,2}$–$1_{1,1}$ | $4_{1,4}$–$3_{1,3}$ | $5_{1,5}$–$4_{1,4}$ | $5_{2,4}$–$4_{2,3}$ |
| NGC 1333-IRAS 4A | $1.0^{+0.7}_{-0.4}$ | $0.5^{+1.2}_{-0.4}$ | $1.2^{+9.9}_{-0.7}$ | <2 |
| NGC 1333-IRAS 4B | - | - | $0.9^{+1.3}_{-0.5}$ | <0.5 |
| NGC 1333-IRAS 2 | $1.1^{+1.9}_{-0.6}$ | - | $5.5^{+11.1}_{-2.2}$ | <4 |
| L1448-MM | - | - | <2 | - |
| L1448-N | $0.4^{+1.1}_{-0.3}$ | <0.1 | - | - |
| L1157-MM | - | - | <1.4 | - |

Table 5 summarizes the derived total column densities and rotational temperatures. The column densities range from 2 to $7 \times 10^{13}$ $cm^{-2}$, and the rotational temperatures from 11 to 40 K. The values are both only lower limits to the actual gas temperature and column density, as the gas temperatures can actually be significantly higher in the case of non-LTE conditions, and the derived column density can also be higher in case of optically thick emission. To correct for this effect, the derived column densities were recalculated adopting the average value of opacities quoted in Table 4. The corrected column densities are also reported in Table 5, and range from 0.8 to $2 \times 10^{14}$ $cm^{-2}$.

### 4.3. LVG modeling

In order to derive the physical conditions of the emitting gas under non-LTE conditions, the formaldehyde emission has been modeled using an LVG code[5]. The collisional coefficients from Green (1991) and the Einstein coefficients from the JPL database (Pickett et al. 1998) were used. The LVG code has three free parameters: the column density to line width ratio $\frac{N(H_2CO)}{\Delta v}$ (which regulates the line opacity), the gas temperature $T_{gas}$, and the molecular hydrogen density $n(H_2)$. When the lines are optically thin the line ratios only depend on the latter two parameters. Since we measured only marginally optically thick lines, the gas temperature and density were first constrained based on the line ratios predicted in the case of optically thin lines. The absolute line fluxes predicted by the model were then compared with observations to constrain the $H_2CO$ column density.

The gas temperature and density have been determined by minimizing the $\chi^2_{red}$, defined as:

$$\chi^2_{red} = \frac{1}{N-2} \sum_{1}^{N} \frac{(\text{Observations} - \text{Model})^2}{\sigma^2} \quad (6)$$

where all the observed $H_2CO$ lines were included. Figure 5 show the $\chi^2$ contours. The derived $T_{gas}$ and $n(H_2)$ are reported in Table 5. The $H_2CO$ column densities were then constrained using the observed o-$H_2CO$ $5_{1,5}$–$4_{1,4}$ line flux, under the assumption of optically thin emission.

The derived temperatures are between 30 and 90 K. These temperatures are significantly higher than the rotational temperature, suggesting that the observed transitions are subthermally populated. Indeed, the derived densities support this conclusion, as they vary between 1 and $6 \times 10^5$ $cm^{-3}$. It is remarkable that the density range is so small, but the density estimate is certainly biased because of the choice of

[5] Details on the used LVG code can be found in Ceccarelli et al. (2002).

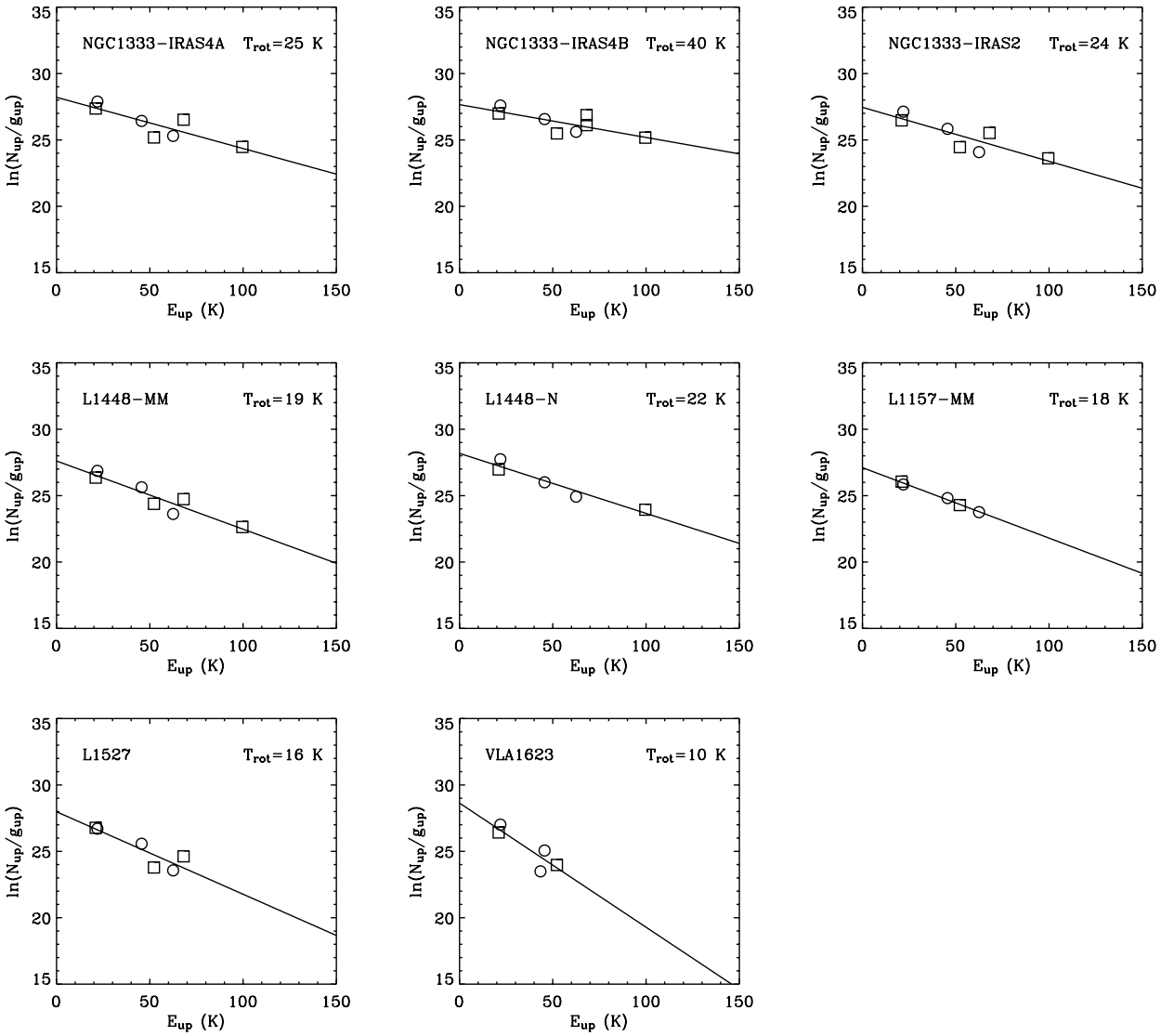


**Fig. 4.** $H_2CO$ rotational diagrams derived for the observed sources. Circles and squares mark the ortho and para $H_2CO$ transitions respectively. Fluxes of the para transitions have been multiplied by the ortho to para ratio, obtained by minimizing the $\chi^2$ between the observations and the predictions of the rotational diagram (see text). Solid lines show the best fit curves.

the transitions. In particular, the densities are slightly lower than those found by Blake et al. (1995) and van Dishoeck et al. (1995) for NGC 1333-IRAS 4A, NGC 1333-IRAS 4B, and IRAS 16293-2422. This is probably due to the fact that those studies included only the higher frequency lines whereas we here included also lower frequency, and thus lower critical density lines. This re-inforces the conclusion that a range of densities are present in the envelope, as predicted by the power-law density structure derived from continuum observations (Jørgensen et al. 2002). Finally, the $H_2CO$ column densities derived with the rotational diagram method are typically lower by less than a factor 5 than the ones derived using the LVG method with the exception of NGC 1333-IRAS 2.

Table 5 also reports estimates of the average $H_2CO$ abundance in each source, obtained dividing the $H_2CO$ by the $H_2$ column densities derived by Jørgensen et al. (2002) from submillimeter continuum observations. The latter refer to the amount of material with a temperature larger than 10 K, typically at a distance of several thousands of AUs, more than the envelope encompassed by the beam of our observations. This material is likely an upper limit to the column density of the gas emitting the $H_2CO$ lines, but it provides a first approximate estimate of the $H_2CO$ abundance. Table 5 shows rather large variations in the $H_2CO$ abundance from source to source. Given the approximation of the method used to derive them, this spread may not be entirely real. In the next section we analyze the observed lines by means of an accurate model that takes into account the source structure.

## 5. Protostellar envelope model

### 5.1. Model description

The model used computes the line emission from a spherical envelope. Dust and gas have density and temperature gradients, that are approximated as follows. The density profile is described by a power law $n(H_2) \propto r^{-\alpha}$, where $\alpha$ is between 0.5

**Table 5.** Results of the rotational diagram and LVG analysis.

| Source | Rotational Diagram | | | LVG | | | | |
|---|---|---|---|---|---|---|---|---|
| | $T_{rot}$ (K) | $N_{thin}(H_2CO)$ ($cm^{-2}$) | $N(H_2CO)^a$ ($cm^{-2}$) | $T_{gas}$ (K) | $n(H_2)$ ($cm^{-3}$) | $N(H_2CO)^b$ ($cm^{-2}$) | $H_2CO/H_2{}^c$ | $CO/H_2{}^d$ |
| NGC 1333-IRAS 4A | 25 | $7 \times 10^{13}$ | $2 \times 10^{14}$ | 50 | $3 \times 10^5$ | $1 \times 10^{15}$ | $5 \times 10^{-10}$ | $8 \times 10^{-6}$ |
| NGC 1333-IRAS 4B | 40 | $7 \times 10^{13}$ | $2 \times 10^{14}$ | 80 | $3 \times 10^5$ | $2 \times 10^{14}$ | $7 \times 10^{-10}$ | $1 \times 10^{-5}$ |
| NGC 1333-IRAS 2 | 24 | $3 \times 10^{13}$ | $1 \times 10^{14}$ | 70 | $3 \times 10^5$ | $5 \times 10^{13}$ | $1 \times 10^{-10}$ | $2 \times 10^{-5}$ |
| L1448-MM | 19 | $2 \times 10^{13}$ | - | 30 | $3 \times 10^5$ | $6 \times 10^{13}$ | $4 \times 10^{-10}$ | $4 \times 10^{-5}$ |
| L1448-N | 22 | $5 \times 10^{13}$ | $8 \times 10^{13}$ | 90 | $1 \times 10^5$ | $3 \times 10^{13}$ | $7 \times 10^{-10}$ | - |
| L1157-MM | 18 | $1 \times 10^{13}$ | - | 80 | $3 \times 10^5$ | $4 \times 10^{13}$ | $3 \times 10^{-11}$ | $6 \times 10^{-6}$ |
| L1527 | 16 | $3 \times 10^{13}$ | - | 30 | $6 \times 10^5$ | $4 \times 10^{13}$ | $1 \times 10^{-9}$ | $4 \times 10^{-5}$ |
| VLA1623 | 11 | $3 \times 10^{13}$ | - | 80 | $1 \times 10^5$ | $8 \times 10^{13}$ | $3 \times 10^{-10}$ | $2 \times 10^{-4}$ |

[a] Corrected for opacity effects, assuming a value of $\tau = 1$ for NGC 1333-IRAS 4A, NGC 1333-IRAS 4B and NGC 1333-IRAS 2 and $\tau = 0.4$ for L1448-N respectively (see Table 4).
[b] Averaged over a 10″ beam.
[c] From $H_2$ column densities quoted by Jørgensen et al. (2002).
[d] From Jørgensen et al. (2002).

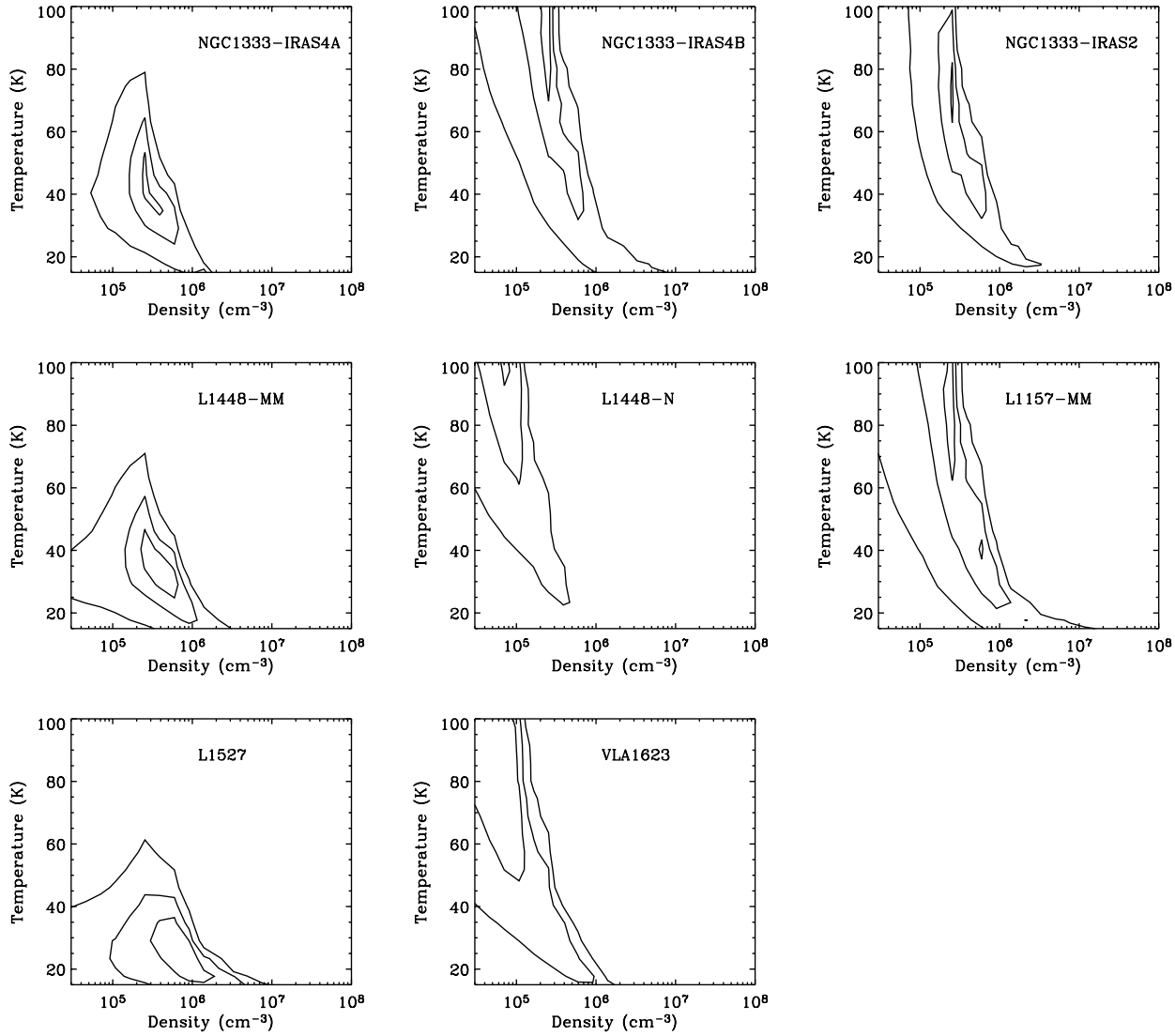


**Fig. 5.** $\chi^2$ contours as a function of the density and temperature of the emitting gas. Contours indicates the 1, 2 and 3$\sigma$ confidence levels respectively.

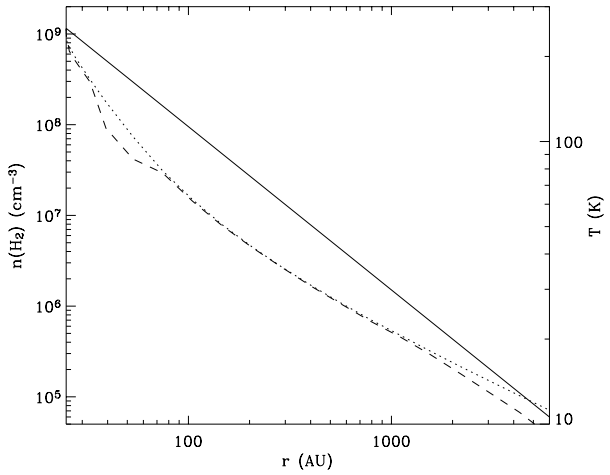


**Fig. 6.** Density (solid line), gas (dashed line) and dust (dotted line) temperature across the envelope of NGC 1333-IRAS 2.

and 2. The case $\alpha = 1.5$ corresponds to an entirely free-falling envelope, whereas $\alpha = 2$ would mimic an isothermal sphere in hydrostatic equilibrium. The densities and dust temperature profiles of all the sources of the sample have been derived by Jørgensen et al. (2002), except for L1448-N, whose analysis is reported in Appendix A.

The gas temperature profile has then been computed by using the model developed by Ceccarelli et al. (1996), which solves the thermal balance in the envelope. In order to compute the gas temperature, one needs to solve the radiative transfer of the main coolants of the gas, i.e. $H_2O$, CO and O. For the water abundance in the inner and outer regions we used the values derived by the analysis of IRAS 16293-2422 (Ceccarelli et al. 2000a) and NGC 1333-IRAS 4 (Maret et al. 2002): $4 \times 10^{-6}$ and $4 \times 10^{-7}$ respectively. The CO abundance in the outer region is taken to be $10^{-5}$ (e.g. Jørgensen et al. 2002), lower than the canonical value, as this species is depleted in the cold parts of the envelope. Finally, the oxygen abundance is taken to be $2.5 \times 10^{-4}$. Figure 6 shows as a typical example the case of NGC 1333-IRAS 2. The gas temperature tracks closely, but not completely, the dust temperature. In the very inner region the gas is colder than the dust because of the increase of the water abundance caused by the icy mantle evaporation (when $T_{\rm dust} \geq 100$ K), which increases the gas cooling capacity. In the very outer region the gas is colder than the dust too, because of the efficient gas cooling by the CO lines (see also the discussion in Ceccarelli et al. 1996; Maret et al. 2002). These differences concern however small regions in the envelope, and therefore the results would be essentially the same if the gas and dust temperature are assumed to be equal. To fully quantify this effect, we ran a model for NGC 1333-IRAS 2 with a gas temperature equal to the dust one, and no significant differences were found.

The velocity field, which regulates the line opacity in the inner envelope, has been approximated as due to free falling gas towards a 0.5 $M_\odot$ central object in all sources (no turbulent broadening is taken into account). In view of the importance of ice evaporation, the formaldehyde abundance across the envelope has been modeled by a step function: when the dust temperature is lower than the ice mantle evaporation ($T_{\rm dust} \leq 100$ K) the abundance has the value $X_{\rm out}$, whereas it increases to $X_{\rm in}$ in the $T_{\rm dust} \geq 100$ K region. Finally, a $H_2CO$ ortho to para ratio of 3 was assumed[6]. We will discuss the dependence of the obtained results on these "hidden" parameters in the next section.

Finally, the line emission is computed by solving the radiative transfer in presence of warm dust in the escape probability formalism where the escape probability $\beta$ is computed at each point of the envelope by integrating the following function over the solid angle $\Omega$ (Ceccarelli et al. 1996):

$$\beta = \frac{k_{\rm d}}{k_{\rm L}+k_{\rm d}} + \frac{k_{\rm L}}{(k_{\rm L}+k_{\rm d})^2} \int {\rm d}\mu \frac{1-\exp\left[-(k_{\rm L}+k_{\rm d})\,\Delta L_{\rm th}\right]}{\Delta L_{\rm th}} \quad (7)$$

where $k_{\rm L}$ and $k_{\rm d}$ are the line and dust absorption coefficients respectively, and $\Delta L_{\rm th}$ is the line trapping region, given by the following expressions:

$$\Delta L_{\rm th} = 2\Delta v_{\rm th} \left( \frac{v}{r} \left| 1 - \frac{3}{2}\mu^2 \right| \right)^{-1} \quad (8)$$

in the infalling region of the envelope (where $\arccos(\mu)$ is the angle with the radial outward direction) and

$$\Delta L_{\rm th} = r\left(1 - \frac{r}{R_{\rm env}}\right) \quad (9)$$

in the static region (where $R_{\rm env}$ is the envelope radius). In the previous equations, $\Delta v_{\rm th}$ is the thermal velocity width and $v$ is the infall velocity. In practice, the photons emitted by the dust can be absorbed by the gas and can pump the levels of the formaldehyde molecules. At the same time, photons emitted by the gas can be absorbed by the dust (at the submillimeter wavelengths the dust absorption is however negligible).

### 5.2. Results

In order to constrain the inner and outer formaldehyde abundance in the envelope, we run a grid of models, varying $X_{\rm out}$ between $10^{-12}$ and $10^{-8}$, and $X_{\rm in}$ between $10^{-12}$ and $10^{-4}$ respectively for each source. Both parameters were constrained by minimizing the $\chi^2_{\rm red}$. The best fit model for each source was then obtained from the $\chi^2_{\rm red}$ diagrams shown in Fig. 7, and the parameters are summarized in Table 6. The list of predicted o-$H_2CO$ spectra for each source are reported in Appendix B.

$X_{\rm out}$ is well constrained in all sources, and varies between $8 \times 10^{-11}$ and $8 \times 10^{-10}$. These values differ on average by a factor 3 from the abundances derived by the LVG analysis. In four sources (NGC 1333-IRAS 4B, NGC 1333-IRAS 2, L1448-MM and L1527) the value of $X_{\rm in}$ is also well constrained by the observations, with a $3\sigma$ confidence level. In three sources (NGC 1333-IRAS 4A, L1448-N and L1157-MM) we also detected formaldehyde abundance jumps, but the level of confidence is less or equal to $2\sigma$. VLA1623 is the only source where no evidence of a jump is detected, although the

[6] Since the value of 2 obtained with the rotational diagrams is highly uncertain, we prefer to adopt the canonical value of 3 for the standard model. We will show in Sect. 5.3.3 that the results are not substantially affected by this value.

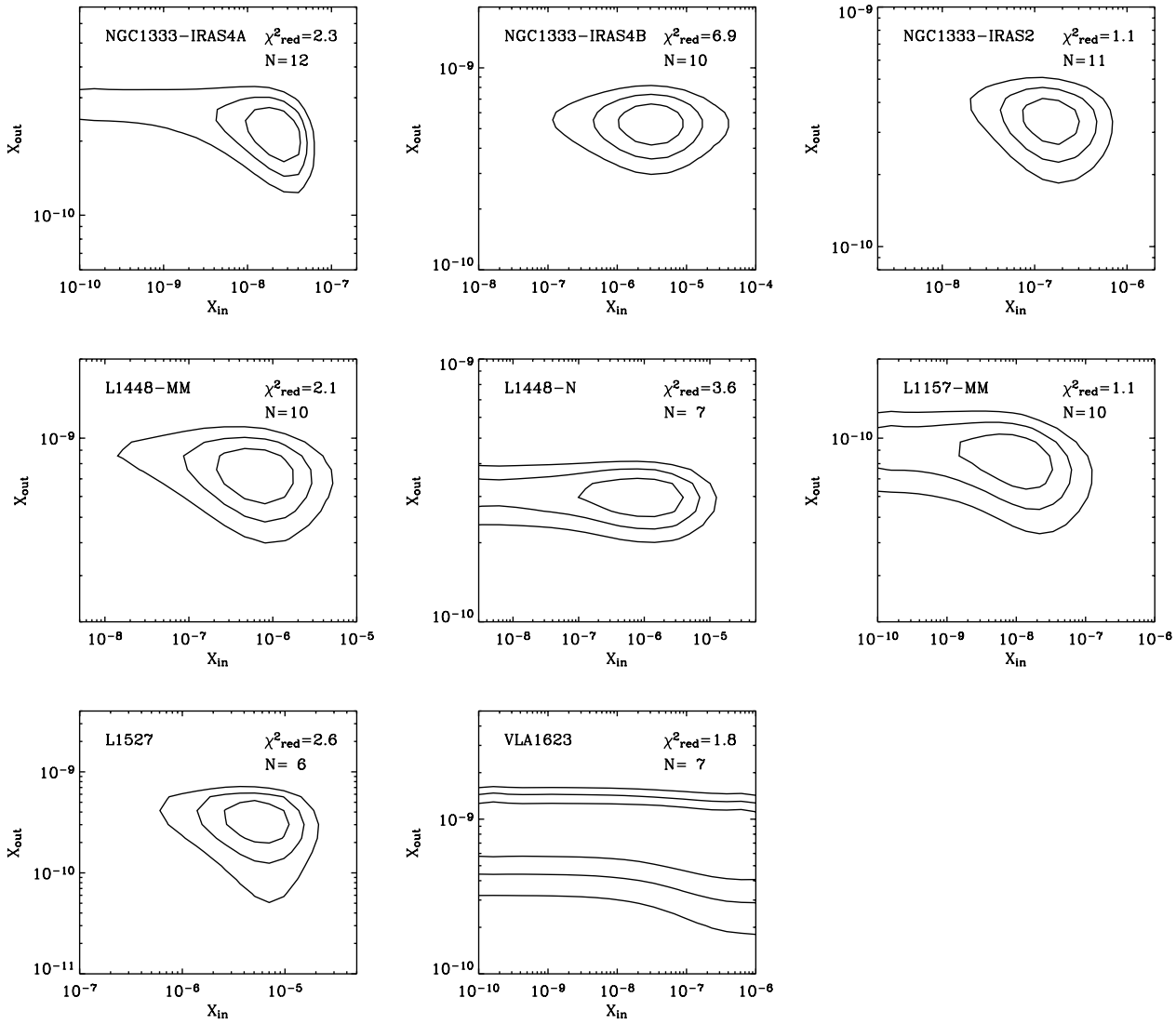


**Fig. 7.** Protostellar envelope model $\chi^2_{\rm red}$ contours as a function of the outer and inner $H_2CO$ abundances. The contours levels show the 1, 2, and $3\sigma$ confidence levels respectively.

**Table 6.** Formaldehyde abundances as derived from the envelope model in the outer parts of the envelope ($X_{\rm out}$) and the inner parts of the envelope ($X_{\rm in}$). The table also includes the radius where the dust temperature is 100 K and 50 K, and the density at the radius where the dust temperature is 100 K.

| Source | $R_{100\ \rm K}$ (AU) | $R_{50\ \rm K}$ (AU) | $n_{100\ \rm K}$ ($\rm cm^{-3}$) | $X_{\rm out}$ | $X_{\rm in}$ |
|---|---|---|---|---|---|
| NGC 1333-IRAS 4A | 53 | 127 | $2 \times 10^9$ | $2 \times 10^{-10}$ | $2 \times 10^{-8}$ |
| NGC 1333-IRAS 4B | 27 | 101 | $2 \times 10^8$ | $5 \times 10^{-10}$ | $3 \times 10^{-6}$ |
| NGC 1333-IRAS2 | 47 | 153 | $3 \times 10^8$ | $3 \times 10^{-10}$ | $2 \times 10^{-7}$ |
| L1448-MM | 20 | 89 | $2 \times 10^8$ | $7 \times 10^{-10}$ | $6 \times 10^{-7}$ |
| L1448-N | 20 | 95 | $1 \times 10^8$ | $3 \times 10^{-10}$ | $1 \times 10^{-6}$ |
| L1157-MM | 40 | 105 | $8 \times 10^8$ | $8 \times 10^{-11}$ | $1 \times 10^{-8}$ |
| L1527 | 20 | 140 | $3 \times 10^6$ | $3 \times 10^{-10}$ | $6 \times 10^{-6}$ |
| VLA1623 | 13 | 48 | $2 \times 10^8$ | $8 \times 10^{-10}$ | - |
| IRAS16293-2422[a] | 133 | 266 | $1 \times 10^8$ | $1 \times 10^{-9}$ | $1 \times 10^{-7}$ |

[a] From Ceccarelli et al. (2000c).

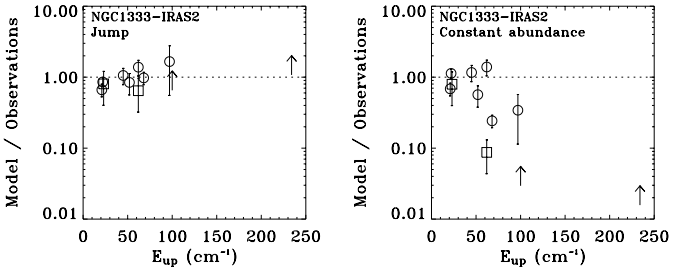


**Fig. 8.** Ratio of the model predictions over the observed fluxes of $H_2CO$ lines as a function of the upper energy of the line, for NGC 1333-IRAS 2. In the left panel a jump in the abundance (Table 6) is adopted, while the in the right panel a constant abundance across the envelope is assumed. The circles and the squares represent $H_2^{12}CO$ and $H_2^{13}CO$ lines respectively. The arrows represent lower limits.

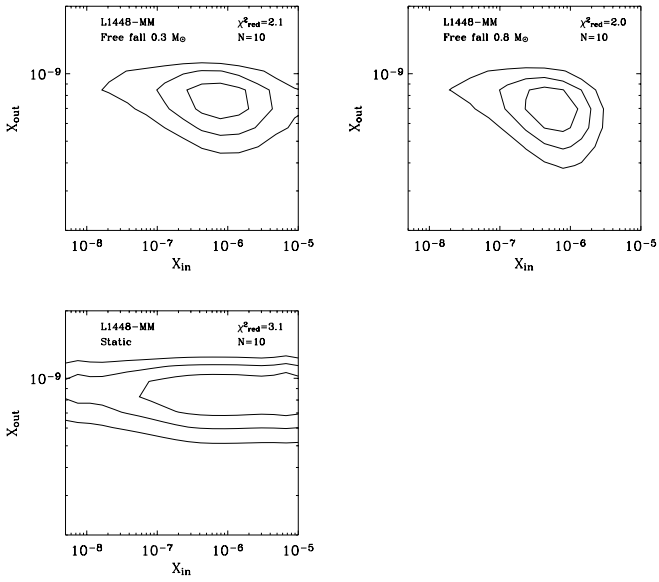


**Fig. 9.** $\chi^2_{\rm red}$ diagrams of L1448-MM for three different velocity profiles. The upper left and upper right panels show the $\chi^2_{\rm red}$ contours derived for a free falling envelope with a central mass of 0.3 and 0.8 $M_\odot$ respectively. The lower panel shows the static envelope case, with a 1 km s$^{-1}$ turbulent velocity. Contours indicate the 1, 2 and 3$\sigma$ confidence levels respectively.

data would not be inconsistent with it. The measured $X_{\rm in}$ values are between $1 \times 10^{-8}$ and $6 \times 10^{-6}$, and the jumps in the formaldehyde abundance are between 100 and $10^4$.

To illustrate the reliability of the derived jumps, Fig. 8 shows the ratio between the model and the observations in the cases of no abundance jump and with a jump, for NGC 1333-IRAS 2 as an example. The constant abundance model can reproduce the observed fluxes of the lower transitions well, but it definitively underestimates the flux of the lines originating from the higher levels.

In the next section, we discuss the effects of the other model parameters on the $H_2CO$ abundance determination.

### *5.3. Dependence on other parameters of the model*

The derived formaldehyde abundances depend on four hidden parameters: the adopted velocity and density profiles, the $H_2CO$ ortho to para ratio and the evaporation temperature. In the following we discuss the influence of all these parameters on the determination of the $H_2CO$ inner abundance.

#### 5.3.1. Velocity profile

In our analysis, we assumed a velocity profile of a free falling envelope, given by:

$$v(r) = \left(\frac{2GM}{r}\right)^{1/2} \quad (10)$$

where $G$ is the gravitational constant and $M$ the mass of the central star. The choice of a free falling velocity profile seems natural, as these protostars are believed to be in accretion phase (e.g. André et al. 2000). Yet, the central mass is a poorly constrained parameter. Recently, Maret et al. (2002) and Ceccarelli et al. (2000a) derived a central mass of 0.5 and 0.8 $M_\odot$ for NGC 1333-IRAS 4A and IRAS 16293-2422 respectively. Here we adopt a central mass of 0.5 $M_\odot$ for all the observed sources, but this parameter could vary from one source to the other.

A different choice for the velocity profile could change the derived abundance. In particular, a higher central mass would imply a higher velocity gradient in the central parts of the envelope, and as a consequence, a lower opacity of the $H_2CO$ lines. This lower opacity would decrease the formaldehyde abundance needed to reproduce a given flux. These differences are expected to affect mainly the high lying lines, which originate in the inner parts of the envelope.

In order to quantify this effect on the derived formaldehyde abundances, two models of L1448-MM were run, using a central mass of 0.3 and 0.8 $M_\odot$ respectively. A third model was also run to check the case of a static envelope, where a turbulent line broadening of 1 km s$^{-1}$ has been added. This model was adopted by Jørgensen et al. (2002), and reproduced well the observed low J CO emission, which originates in the static envelope.

Figure 9 shows the $\chi^2_{\rm red}$ diagrams obtained in the three cases. While the derived outer formaldehyde abundance is not much affected by the adopted velocity field, the inner abundance changes significantly when adopting a static envelope rather than a free-fall profile. Yet, the inner abundance is well constrained in the first two cases (free-fall with different central masses), and very weakly depends on the adopted central mass: $8 \times 10^{-7}$ and $5 \times 10^{-7}$ for 0.3 and 0.8 $M_\odot$ respectively. On the contrary, only a lower limit is obtained if a static envelope is adopted: $>3 \times 10^{-8}$. This is due to different line opacities in the three cases. In a static envelope, the high lying lines become more easily optically thick, because of the reduced linewidth with respect to the free-fall cases. For this reason, these lines do not depend on $X_{\rm in}$, when $X_{\rm in}$ is $\sim 10^{-7}$, because they become optically thick. This explains why only a lower limit on $X_{\rm in}$ can be computed in that case.

### 5.3.2. Density profile

The $H_2CO$ abundances depend on the density profile derived from the continuum observations. In particular, the observations used to derive the physical structure of the envelopes have been obtained with a typical beamwidth of 10″, i.e. 2200 AU at the distance of NGC 1333. The observed continuum is therefore not very sensitive to the physical conditions in the innermost regions of the envelope, at scales smaller than a few hundred AUs. Consequently, the derived density power-law index reflects rather the density in the outer part of the envelope, and the inner density, extrapolated from these power law, may be a rough estimate. Finally, the determination of the density profiles of some of the sources of the sample was difficult because of the existence of multiple components (Jørgensen et al. 2002). Jørgensen et al. (2002) reported an average uncertainty of ±0.2 on the power-law index. If the density at the outer radius of the envelope is assumed to be correctly determined by the continuum observations, the uncertainty on the power-law index corresponds to an uncertainty of a factor five on the density at the inner radius of the envelope. In order to check the effect of this uncertainty on the derived abundances, we ran models of NGC 1333-IRAS 4B with an inner density artificially multiplied by a factor 5 (note that the outer density is not changed). Whereas the $H_2CO$ outer abundance remains unchanged, the inner abundance decreases by about the same factor 5. Uncertainties in the inner density could therefore lead to uncertainties on the derived inner abundances of the same order of magnitude.

### 5.3.3. The $H_2CO$ ortho to para ratio

The derived formaldehyde abundances depend also on the value of the $H_2CO$ ortho to para ratio. Given the relatively low number of observed lines, this parameter cannot be constrained by the present observations. Actually, it is very badly constrained even in the case of IRAS 16293-2422, where many more formaldehyde lines have been observed. Ceccarelli et al. (2000c) and Schöier et al. (2002) report a value for the ortho and para ratio around 3, but with a large uncertainty. We thus adopted the canonical value of 3 in our analysis (Kahane et al. 1984).

As an example, Fig. 10 shows the influence of this parameter on the derived $H_2CO$ abundance of NGC 1333-IRAS 4A. We ran models with the ortho to para ratio 1, 2 and 3 respectively. While the derived inner and outer abundances are almost identical for the three ratios, the abundance jump is slightly better constrained for a ratio of 1 ($3\sigma$) than an higher ratio ($2\sigma$).

### 5.3.4. Evaporation temperature

Finally, the evaporation temperature $T_{\rm ev}$, at which the formaldehyde desorption occurs, is also a hidden parameter of our model. As described in Sect. 5.1, in the present study we adopted $T_{\rm ev} = 100$ K, which corresponds to the evaporation of water ices (Aikawa et al. 1997). However, part of the desorption could also occur at the evaporation temperature of pure formaldehyde ices (50 K; Aikawa et al. 1997; Rodgers & Charnley 2003). For example, a detailed analysis of the formaldehyde spatial emission in IRAS 16293-2422 has shown that the formaldehyde abundance has a first jump, of about a factor 10, where $T_{\rm dust} \geq 50$ K, and a second jump of about a factor 25 where $T_{\rm dust} \geq 100$ (Ceccarelli et al. 2001). However, given the relatively small number of observed lines and the absence of spatial information on the formaldehyde emission in the source sample of the present study, we limited the $H_2CO$ abundance profile to a single step function. In order to check if the data are also consistent with a jump at 50 K, a model with a jump in the abundance at 50 K for NGC 1333-IRAS 2 was run (see Fig. 11). While $X_{\rm out}$ is very little sensitive to this parameter, $X_{\rm in}$ is about ten times smaller when assuming a jump at 50 K ($2 \times 10^{-7}$ and $2 \times 10^{-8}$ for 100 and 50 K respectively). We note, however, that the best agreement with the data is obtained for an evaporation temperature of 100 K ($\chi^2_{\rm red} = 1.1$ against 2.3 respectively).

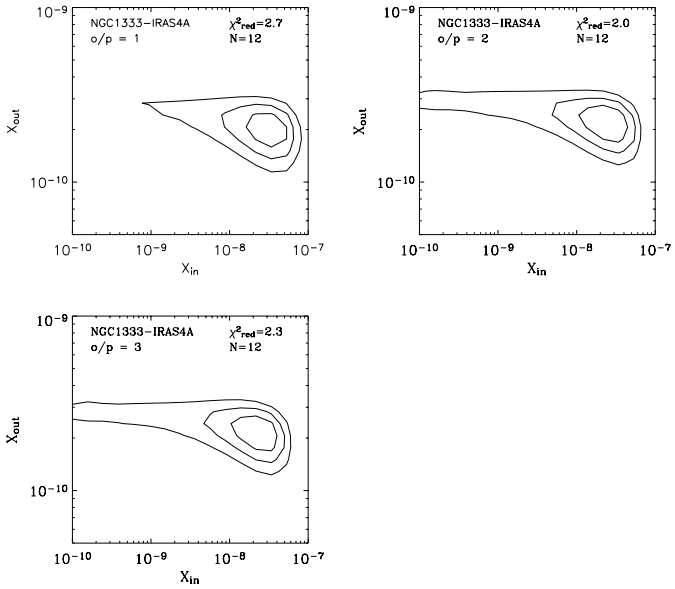


**Fig. 10.** $\chi^2_{\rm red}$ diagrams of NGC 1333-IRAS 4 for three different ortho to para ratios. The upper left, upper right and lower panels shows the $\chi^2_{\rm red}$ contours derived for an ortho to para ratio of 1, 2 and 3 respectively. Contours indicates the 1, 2 and $3\sigma$ confidence levels respectively.

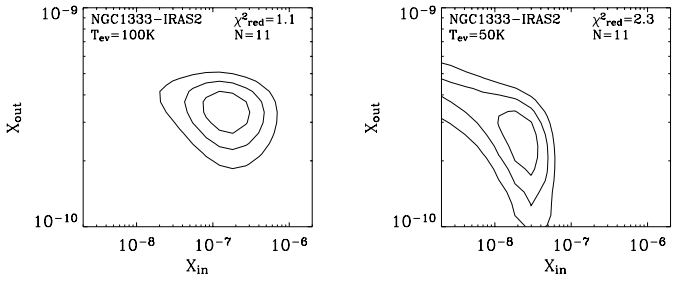


**Fig. 11.** $\chi^2_{\rm red}$ diagrams of NGC 1333-IRAS 2 for an evaporation temperature of 100 K (*left panel*) and 50 K (*right panel*). Contours indicates the 1, 2 and $3\sigma$ confidence levels respectively.

### 5.3.5. Summary

In the $\chi^2_{\rm red}$ analysis of Sect. 5.2, we adopted the most reasonable values of the various hidden parameters in the model. In this section we have explored the effect of variations in them on the derived abundance jumps. We emphasize that the actual value of the jump as well as the precise location are quite uncertain. Based on the previous analysis, the adopted velocity field seems to affect most strongly the amplitude and/or the presence of the derived jump, in particular when a static, turbulent field is considered. The other three parameters, the inner density, the ortho to para ratio, and the evaporation temperature seem to play a minor role. In this sense, the model assumption of an infalling envelope is probably the most critical in the present analysis. As already mentioned, we favor the hypothesis of collapsing envelopes, both because evidences are accumulating in this direction (e.g. Di Francesco et al. 2001), and because it is the most natural one.

To summarize, the sources (i.e. NGC 1333-IRAS 4B, NGC 1333-IRAS 2, L1448-MM and L1527) where the $\chi^2_{\rm red}$ analysis yields $3\sigma$ evidence for jumps, the presence of an abundance jump is rather firm in our opinion. Although more marginal, the data are consistent with the presence of a jump in the other surveyed sources as well. Appendix B lists the predicted fluxes of the brightest ortho formaldehyde lines. Predictions of para $H_2CO$ line fluxes can be found on the web site MEPEW[7] (Ceccarelli et al. 2003). In particular, the submillimeter lines are sensitive to the presence and amplitude of the jump in the $H_2CO$ abundance, and future observations with existing (JCMT, CSO) and future (e.g. SMA, ALMA) submillimiter telescopes will better constrain this value.

## 6. Discussion

The first remarkable and by far the most important result of this study is the evidence for a region of formaldehyde evaporation in seven out of eight observed sources. In these regions, the formaldehyde abundance jumps to values two or more orders of magnitude larger than the abundance in the cold outer envelope. The transition is consistent with the location where the dust temperature reaches 100 K. The radius of these warm regions is between 13 and 133 AU, and the densities[8] are between 1 and $20 \times 10^8$ cm$^{-3}$. A straightforward interpretation of this result is that the grain mantles sublimate at 100 K, releasing into the gas phase their components, and, among them, formaldehyde. In addition, recent observations have shown the presence of complex molecules, typical of massive hot cores (Cazaux et al. 2003) towards IRAS 16293-2422, the first studied hot core of low mass protostars (Ceccarelli et al. 2000a,b,c; Schöier et al. 2002). The similarity with the well studied hot cores of the massive protostars is certainly striking: *warm, dense, and compact regions chemically dominated by the mantle evaporation*.

[7] http://www-laog.obs.ujf-grenoble.fr/~ceccarel/mepew/mepew.html

[8] L1527 is an exception, with a density of $3\times10^6$ cm$^{-3}$, but, as commented by Jørgensen et al. (2002) this may be due to the contribution of the disk, that may dominate the continuum emission in the inner parts of this source (Loinard et al. 2002b).

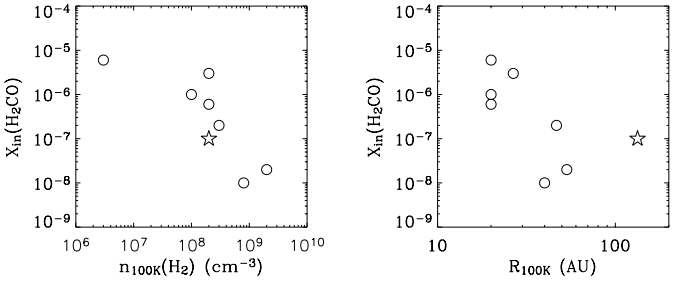


**Fig. 12.** Derived $H_2CO$ $X_{\rm in}$ abundances as a function of the density (*left panel*) and the radius (*right panel*) where $T_{\rm dust}$ = 100 K. The star represent IRAS 16293-2422.

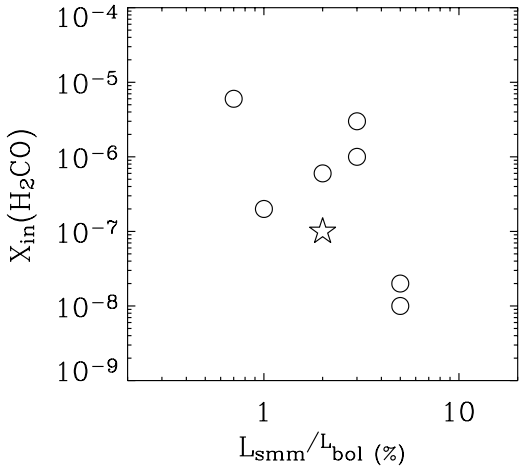


**Fig. 13.** Derived $H_2CO$ $X_{\rm in}$ abundances as a function of $L_{\rm smm}/L_{\rm bol}$. The star represent IRAS 16293-2422.

Even though the chemistry can be, and very probably is different in high and low mass protostars, the hot cores represent basically the same process in both type of sources. Our study does not address the possibility that some of the $H_2CO$ ice mantles may be liberated by shocks interacting with the inner envelope, since the line wings have been excluded from our analysis. The role of shocks could be studied by future high angular resolution maps of the line center and line wing emission.

### 6.1. $X_{in}$ versus $L_{smm}/L_{bol}$

The $H_2CO$ abundance in the inner region shows a loose trend with a variety of source characteristics. These include the density in the inner region and the size of the region (Fig. 12), as well as the ratio of the submillimeter luminosity to the bolometric luminosity, $L_{\rm smm}/L_{\rm bol}$ (Fig. 13). In assessing these correlations, we should, of course, keep the large uncertainties – an order of magnitude – as well as systematic effects in mind. In particular, underestimating the density will immediately result in overestimating the abundance required to explain the observations (cf. Sect. 5.3). Likewise, if we underestimate the size of the emitting region, we will need a higher $H_2CO$ abundance. Now, which of these, if any, correlations is the prime correlation and which one is derived is not directly clear. In particular, within the inside-out-collapse, the density and inner radius are anti-correlated as are the luminosity and the radius of the evaporated region.

The apparent anti-correlation between the $H_2CO$ abundance and $L_{smm}/L_{bol}$ (Fig. 13) is of particular interest. The latter is generally taken as an indicator of the evolutionary stage of the protostar where a larger value for $L_{smm}/L_{bol}$ implies "youth" (e.g. large amounts of cold material surrounding the YSO). The anti-correlation may seem a surprising result, as the most accepted scenario predicts that formaldehyde is formed on the grain surfaces, likely by successive hydrogenation of CO (Tielens & Hagen 1982; Charnley et al. 1997) during the pre-stellar phase. Once in the gas phase because of the evaporation of the grain mantles, formaldehyde is destroyed (i.e. converted into more complex molecules) on a timescale of $\sim 10^4$ yr (Charnley et al. 1992). In this picture, the youngest sources should have the largest $X_{in}$, which is evidently not the case. This picture, however, might be somewhat over-simplified. Indeed, the process of ice evaporation is continuous, involving larger and larger regions as the time passes and the luminosity of the protostar increases – as pointed out by the models by Ceccarelli et al. (1996) and Rodgers & Charnley (2003) – so that the result is a shell of continuously refurbished $H_2CO$, moving outwards. The main point is that the region of formaldehyde overabundance never disappears, but just moves, and the jump in the $H_2CO$ abundance is only governed by the quantity of formaldehyde in the grain mantles.

If the $L_{smm}/L_{bol}$ ratio is not an age indicator but rather a parameter affected more by the different initial conditions of each protostar, and specifically it is larger in sources where the pre-stellar density is larger (e.g. Jayawardhana et al. 2001), the trend of Fig. 13 would imply that the $H_2CO$ ice abundance depends on the pre-stellar conditions. Less dense pre-stellar conditions (i.e. lower $L_{smm}/L_{bol}$ ratios) would give rise to more $H_2CO$ enriched ices, because there is more atomic H and thus more grain surface hydrogenation to form $H_2CO$. This is indeed consistent with the fact that the efficiency of CO hydrogenation into $H_2CO$ on the grain mantles is ~250 times larger in $H_2O$-rich ices when compared to CO-rich ices (Ceccarelli et al. 2001). And since less dense regions have likely more $H_2O$-rich than CO-rich ices, because CO-rich ices likely form in relatively dense condensations (Bacmann et al. 2002), the larger $H_2CO$ abundance in sources with a lower $L_{smm}/L_{bol}$ would therefore be due to a real larger efficiency of the $H_2O$-rich ices in forming $H_2CO$. As a consequence, our finding would suggest that the $L_{smm}/L_{bol}$ ratio does not probe the evolutionary status of protostars, but rather mainly reflects their different initial conditions.

Alternative explanations are also possible. For example, recent laboratory works suggest that the formation of formaldehyde by CO hydrogenation on the grains depends on the dust temperature (Watanabe et al. 2003), and this may also be consistent with "older" protostars (i.e. lower $L_{smm}/L_{bol}$ ratios), being also hotter, having larger $H_2CO$ abundances. This, of course, would imply that the bulk of the $H_2CO$ is formed in a stage later than the CO condensation, namely during the pre-stellar core phase (Bacmann et al. 2002). Whether this is likely is difficult to say, for CO may indeed be trapped on the grain mantles and partly converted into $H_2CO$ only when the grain temperature increases, as suggested by the laboratory experiments. Another possibility is that formaldehyde formation on grains needs UV radiation (e.g d'Hendecourt et al. 1986; Schutte et al. 1996). Analogously to above, formaldehyde would be formed only in a later stage, and the older the protostar, the larger the UV field and the larger the $H_2CO$ abundance.

All these interpretations need to be taken with caution, of course, since the inferred variations in the inner $H_2CO$ abundance might reflect uncertainties in the density and/or size of the region emitting the $H_2CO$ lines. A similar study on a larger sample and focussing on higher energy lines is required to draw more definitive conclusions.

### 6.2. Low versus high mass protostars

In Sect. 5 we have examined the evidence for the presence of jumps in the $H_2CO$ abundance in the warm gas surrounding low mass YSOs. The presence of such abundance jumps in hot cores around high mass stars is not well established. On the one hand, the prototype of hot cores in regions of massive star formation – the hot core in the Orion BN/KL region – has a $H_2CO$ abundance of $10^{-7}$ (Sutton et al. 1995). On the other hand, in a study of hot cores in a sample of massive protostars, van der Tak et al. (2000) did not find evidence for the presence of $H_2CO$ abundance jumps, but did find evidence for jumps in the $CH_3OH$ abundance. It is unclear at present whether the Orion hot core or the van der Tak sample is more representative for the composition of hot cores in regions of massive star formation. Presuming that the differences in $H_2CO$ abundance jumps are real, we note that the composition of the ices – which drive the chemistry in hot cores – may well differ between regions of low mass and high mass star formation.

Supporting this idea, the deuterium fractionation is dramatically different in the high and low mass protostars. Doubly deuterated formaldehyde and methanol have been observed to be extremely abundant in low mass protostars when compared to massive protostars. The $D_2CO/H_2CO$ ratio is more than 25 times larger in low than in high mass protostars (Ceccarelli et al. 1998; Loinard et al. 2002a). Deuterated methanol may be as abundant than its main isotopomer in the low mass protostar IRAS 16293-2422 (Parise et al. 2002), whereas it is only 4% of $CH_3OH$ in Orion (Jacq et al. 1993). Since this extreme deuteration is likely a grain mantle product (e.g. Ceccarelli et al. 2001; Parise et al. 2002), the dramatic differences in the molecular deuteration between low and high mass protostars are already a very strong indication that mantles in both type of sources are *substantially* different. This indeed does not comes as a surprise, as the pre-collapse conditions very likely differ: warmer in high than in low mass stars, at the very least.

### 6.3. $X_{out}$ versus CO abundance

Finally, Fig. 14 compares the $H_2CO$ abundance $X_{out}$ with the CO abundance derived by Jørgensen et al. (2002), in the outer envelope. On the same plot we also reported the values found in the prestellar cores studied by Bacmann et al. (2002, 2003). The first thing to notice is the similarity of the values found in Class 0 sources and pre-stellar cores, in both molecules, despite the different methods used to derive the abundances.

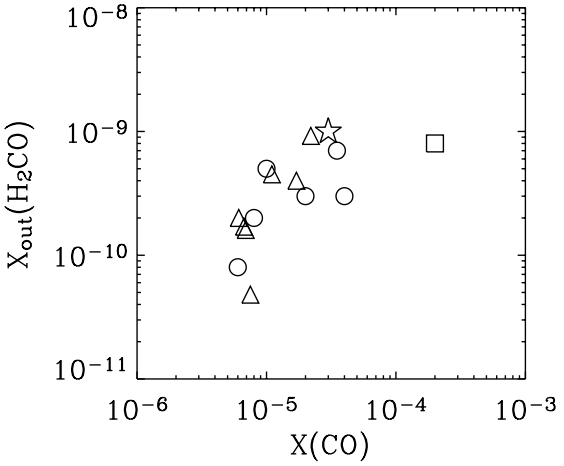


**Fig. 14.** Derived outer formaldehyde abundance $X_{out}$ as a function the CO abundance of the outer enveloppe. Circles represent Class 0 sources, The star represents IRAS 16293-2422, the square represents VLA1623, and the triangles represent the pre-stellar cores of Bacmann et al. (2002, 2003) sample.

The similarity of the values adds support to the thesis that the pre-stellar cores of the Bacmann et al. sample are precursors of Class 0 sources, and that the outer regions of the envelopes of Class 0 sources are formed by material still unchanged by the collapse, i.e. that reflects the pre-collapse conditions. Second aspect to note of Fig. 14 is the clear correlation between the $H_2CO$ and CO abundance. In this case the interpretation is straightforward: in the outer, cold envelope molecules are depleted, and the degree of depletion is the same for the CO and the $H_2CO$ molecules. As discussed in Bacmann et al. (2002), the limited CO depletion observed in pre-stellar cores strongly suggests that a relatively efficient mechanism (cosmic rays?) re-injects CO into the gas phase. Since the binding energies of the CO and $H_2CO$ are relatively different (e.g. Aikawa et al. 1997), the linear correlation of Fig. 14 strengthens the claim that $H_2CO$ molecules are trapped into CO-rich ices (Ceccarelli et al. 2001).

## 7. Conclusions

We have presented a spectral survey of the formaldehyde emission of a sample of eight Class 0 protostars, carried out with the IRAM 30 m and JCMT telescopes. A total of eight transitions were selected for each source, covering a large range of upper level energies in order to probe different physical conditions. When possible, the isotopic lines were observed in order to derive the line opacities. Most of the lines are relatively narrow with a small contribution from wings extending to larger velocities. Using the standard rotational diagram method, we derived rotational temperatures between 11 and 40 K, and $H_2CO$ column densities between $1 \times 10^{13}$ and $7 \times 10^{13}$ cm$^{-2}$. For the sources with detected $H_2^{13}CO$ lines, opacity corrections increase the derived column densities to the range 0.8 and $2 \times 10^{14}$ cm$^{-2}$. In order to test the effect of non-LTE excitation, the observed emission has been modeled using a LVG code. In this way the derived temperatures are significantly higher than the rotational temperatures, suggesting that the observed transitions are sub-thermally populated. The inferred densities, between 1 and $6 \times 10^5$ cm$^{-3}$, indeed support this conclusion.

To take into account the density and temperature gradients in the protostellar envelopes, the emission has been modeled using densities and dust temperature profiles derived from previous studies of the continuum emission of these objects. The gas temperature in the envelopes was computed using a code of the thermal balance for protostellar envelopes. The formaldehyde abundance across the envelope has been approximated by a step function: an outer abundance $X_{out}$ where $T_{dust} \leq 100$ K, and a inner abundance $X_{in}$ at $T_{dust} \geq 100$ K. We show that the outer abundance, $X_{out}$, is well constrained in all the sources, and varies between $8 \times 10^{-11}$ and $8 \times 10^{-10}$. The inner abundance $X_{in}$ is well constrained in four sources with a $3\sigma$ level confidence, while in three sources it is only a $\leq 2\ \sigma$ evidence, and no evidence of a jump is found in VLA1623. The derived values of $X_{in}$ range between $1 \times 10^{-8}$ and $6 \times 10^{-6}$, showing jumps of the formaldehyde abundance between 2 and 4 orders of magnitude. *The most important conclusion of this study is hence that large amounts of formaldehyde are injected into the gas phase when the grain mantles evaporate at 100 K.*

We have discussed the uncertainties on the actual values of the hidden parameters of the model, namely the velocity and density profile, the $H_2CO$ ortho to para ratio, and the evaporation temperature. The uncertainty in these parameters makes the abundance jump value and jump locations uncertain for some sources. Future observations of higher frequency lines and modeling of the line profiles may distinguish between the different interpretations.

We found that sources with lower $L_{smm}/L_{bol}$ ratios possess the largest inner $H_2CO$ abundances. We discussed why we think that this reflects very likely a different $H_2CO$ enrichment of the grain mantles.

We found that the inner $H_2CO$ abundances are systematically larger than the $H_2CO$ abundances of the hot cores of the sample of massive protostars studied by van der Tak et al. (2000). This supports to the idea that low and high mass protostars have a different grain mantle composition.

Finally, the derived outer $H_2CO$ abundance shows a clear correlation with the CO abundance, implying that both molecules are depleted by a similar factor in the outer envelope, namely that $H_2CO$ molecules are likely trapped in CO-rich ices in the outer envelope.

*Acknowledgements.* Most of the computations presented in this paper were performed at the Service Commun de Calcul Intensif de l'Observatoire de Grenoble (SCCI). Astrochemistry in Leiden is supported by a NOVA Network 2 Ph.D. grant and by a NWO Spinoza grant.

## References

Aikawa, Y., Umebayashi, T., Nakano, T., & Miyama, S. M. 1997, ApJ, 486, L51
André, P., Ward-Thompson, D., & Barsony, M. 2000, Protostars and Planets IV, 59
Bachiller, R., & Perez Gutierrez, M. 1997, ApJ, 487, L93
Bacmann, A., Lefloch, B., Ceccarelli, C., et al. 2002, A&A, 389, L6
Bacmann, A., Lefloch, B., Ceccarelli, C., et al. 2003, ApJ, 585, L55

Bergin, E. A., Alves, J., Huard, T., & Lada, C. J. 2002, ApJ, 570, L101
Bernstein, M. P., Sandford, S. A., Allamandola, L. J., et al. 1999, Science, 283, 1135
Blake, G. A., Sandell, G., van Dishoeck, E. F., et al. 1995, ApJ, 441, 689
Blake, G. A., Sutton, E. C., Masson, C. R., & Phillips, T. G. 1987, ApJ, 315, 621
Boogert, A. C. A., Ehrenfreund, P., Gerakines, P. A., et al. 2000a, A&A, 353, 349
Boogert, A. C. A., Tielens, A. G. G. M., Ceccarelli, C., et al. 2000b, A&A, 360, 683
Boogert, A. C. A., Hogerheijde, M. R., Ceccarelli, C., et al. 2002, ApJ, 570, 708
Caselli, P., Hasegawa, T. I., & Herbst, E. 1993, ApJ, 408, 548
Caselli, P., Walmsley, C. M., Terzieva, R., & Herbst, E. 1998, ApJ, 499, 234
Caselli, P., Walmsley, C. M., Zucconi, A., et al. 2002, ApJ, 565, 331
Cazaux, S., Tielens, A. G. G. M., Ceccarelli, C., et al. 2003, ApJ, 539, L51
Ceccarelli, C., Hollenbach, D. J., & Tielens, A. G. G. M. 1996, ApJ, 471, 400
Ceccarelli, C., Caux, E., White, G. J., et al. 1998, A&A, 331, 372
Ceccarelli, C., Castets, A., Caux, E., et al. 2000a, A&A, 355, 1129
Ceccarelli, C., Loinard, L., Castets, A., Faure, A., & Lefloch, B. 2000b, A&A, 362, 1122
Ceccarelli, C., Loinard, L., Castets, A., Tielens, A. G. G. M., & Caux, E. 2000c, A&A, 357, L9
Ceccarelli, C., Loinard, L., Castets, A., et al. 2001, A&A, 372, 998
Ceccarelli, C., Baluteau, J.-P., Walmsley, M., et al. 2002, A&A, 383, 603
Ceccarelli, C., Maret, S., Tielens, A. G. G. M., Castets, A., & Caux, E. 2003, A&A, 410, 587
Cernis, K. 1990, Ap&SS, 166, 315
Charnley, S. B., Tielens, A. G. G. M., & Millar, T. J. 1992, ApJ, 399, L71
Charnley, S. B., Tielens, A. G. G. M., & Rodgers, S. D. 1997, ApJ, 482, L203
Dartois, E., Schutte, W., Geballe, T. R., et al. 1999, A&A, 342, L32
de Jong, T., Boland, W., & Dalgarno, A. 1980, A&A, 91, 68
d'Hendecourt, L. B., Allamandola, L. J., Grim, R. J. A., & Greenberg, J. M. 1986, A&A, 158, 119
Di Francesco, J., Myers, P. C., Wilner, D. J., Ohashi, N., & Mardones, D. 2001, ApJ, 562, 770
Gerakines, P. A., Whittet, D. C. B., Ehrenfreund, P., et al. 1999, ApJ, 522, 357
Gibb, E. L., Whittet, D. C. B., Schutte, W. A., et al. 2000, ApJ, 536, 347
Goldsmith, P. F., & Langer, W. D. 1999, ApJ, 517, 209
Green, S. 1991, ApJS, 76, 979
Ivezic, Z., & Elitzur, M. 1997, MNRAS, 287, 799
Jacq, T., Walmsley, C. M., Mauersberger, R., et al. 1993, A&A, 271, 276
Jansen, D. J., van Dishoeck, E. F., & Black, J. H. 1994, A&A, 282, 605
Jansen, D. J., van Dishoeck, E. F., Black, J. H., Spaans, M., & Sosin, C. 1995, A&A, 302, 223
Jayawardhana, R., Hartmann, L., & Calvet, N. 2001, ApJ, 548, 310
Jørgensen, J. K., Schöier, F. L., & van Dishoeck, E. F. 2002, A&A, 389, 908
Kahane, C., Lucas, R., Frerking, M. A., Langer, W. D., & Encrenaz, P. 1984, A&A, 137, 211
Keane, J. V., Tielens, A. G. G. M., Boogert, A. C. A., Schutte, W. A., & Whittet, D. C. B. 2001, A&A, 376, 254
Kurtz, S., Cesaroni, R., Churchwell, E., Hofner, P., & Walmsley, C. M. 2000, Protostars and Planets IV, 299
Loinard, L., Castets, A., Ceccarelli, C., et al. 2002a, Planet. Space Sci., 50, 1205
Loinard, L., Castets, A., Ceccarelli, C., et al. 2000, A&A, 359, 1169
Loinard, L., Rodríguez, L. F., D'Alessio, P., Wilner, D. J., & Ho, P. T. P. 2002b, ApJ, 581, L109
Mangum, J. G., & Wootten, A. 1993, ApJS, 89, 123
Maret, S., Ceccarelli, C., Caux, E., Tielens, A. G. G. M., & Castets, A. 2002, A&A, 395, 573
Parise, B., Ceccarelli, C., Tielens, A. G. G. M., et al. 2002, A&A, 393, L49
Pickett, H. M., Poynter, R. L., Cohen, E. A., et al. 1998, JQSRT, 60, 830
Rodgers, S. D., & Charnley, S. B. 2003, ApJ, 585, 355
Schöier, F. L., Jørgensen, J. K., van Dishoeck, E. F., & Blake, G. A. 2002, A&A, 390, 1001
Schutte, W. A., Gerakines, P. A., Geballe, T. R., van Dishoeck, E. F., & Greenberg, J. M. 1996, A&A, 309, 633
Shu, F. H., Adams, F. C., & Lizano, S. 1987, ARA&A, 25, 23
Sutton, E. C., Peng, R., Danchi, W. C., et al. 1995, ApJS, 97, 455
Tafalla, M., Myers, P. C., Caselli, P., Walmsley, C. M., & Comito, C. 2002, ApJ, 569, 815
Tafalla, M., Myers, P. C., Mardones, D., & Bachiller, R. 2000, A&A, 359, 967
Tielens, A. G. G. M., & Hagen, W. 1982, A&A, 114, 245
van der Tak, F. F. S., van Dishoeck, E. F., & Caselli, P. 2000, A&A, 361, 327
van Dishoeck, E. F., Blake, G. A., Jansen, D. J., & Groesbeck, T. D. 1995, ApJ, 447, 760
Watanabe, N., Shiraki, T., & Kouchi, A. 2003, ApJ, 588, L121

# Online Material

## Appendix A: Density and temperature profile of L1448-N

The density and temperature profile of L1448-N have been determined following the method used by Jørgensen et al. (2002). The spectral energy distribution (SED) and JCMT-SCUBA maps at 450 and 800 $\mu$m have been compared to the prediction of the radiative code DUSTY[9] (Ivezic & Elitzur 1997). The JCMT observations were taken from the JCMT archive. Figure A.1 shows the result of the fits of the brightness profile and SED of this source. The envelope parameters from this modeling are summarized in Table A.1.

L1448-N shows a relatively flat density profile. This profile may reflect the asymmetry of the source and the extension of the emission, which can flatten the derived profile (see Jørgensen et al. 2002, for a discussion of the effects of asymmetries in the derived density profile).

**Table A.1.** L1448-N best fit parameters from the DUSTY modelling and derived physical parameters.

| DUSTY parameters | |
|---|---|
| $Y$ | 1100 |
| $\alpha$ | 1.2 |
| $\tau_{100}$ | 0.8 |
| **Derived physical parameters** | |
| $R_i$ | 10 AU |
| $R_{10\ \mathrm{K}}$ | 7000 AU |
| $n_{R_i}$ | $4.9 \times 10^8$ cm$^{-3}$ |
| $n_{10\ \mathrm{K}}$ | $1.1 \times 10^5$ cm$^{-3}$ |
| $M_{10\ \mathrm{K}}$ | 2.5 $M_\odot$ |

## Appendix B: Models predictions for formaldehyde lines fluxes

In this Appendix we present the model predictions for the fluxes of selected o-$H_2CO$ transitions. In Table B.1 we report the line fluxes computed assuming a constant abundance $X_{\mathrm{out}}$ across the envelope, while Table B.2 reports the fluxes predicted assuming an abundance $X_{\mathrm{out}}$ in the outer part of the envelope where $T_{\mathrm{dust}} < 100$ K, increasing to $X_{\mathrm{in}}$ in the inner part of the envelopes, at the radius where $T_{\mathrm{dust}} \geq 100$ K. The adopted values of $X_{\mathrm{in}}$ and $X_{\mathrm{out}}$ are the best fit values reported in 6. In these two tables, the line fluxes are expressed in erg s$^{-1}$ cm$^{-2}$. Although a conversion in K km s$^{-1}$ would have been more practical to compare these fluxes with observations, this conversion depends on the telescope used and the extent of the line emission. However if the emitting region is smaller than the telescope beam, the fluxes can be approximatively converted into K km s$^{-1}$ using the conversion factors reported by Ceccarelli et al. (2003).

While low lying lines fluxes are comparable in two tables, higher energy lines fluxes substantially differ. Higher frequency observations can therefore help to distinguish between a constant abundance in the envelope and a jump in the abundance, especially on the sources of our sample for which the jump in the abundance is uncertain.

[9] DUSTY is publicly available at `http://www.pa.uky.edu/~moshe/dusty/`

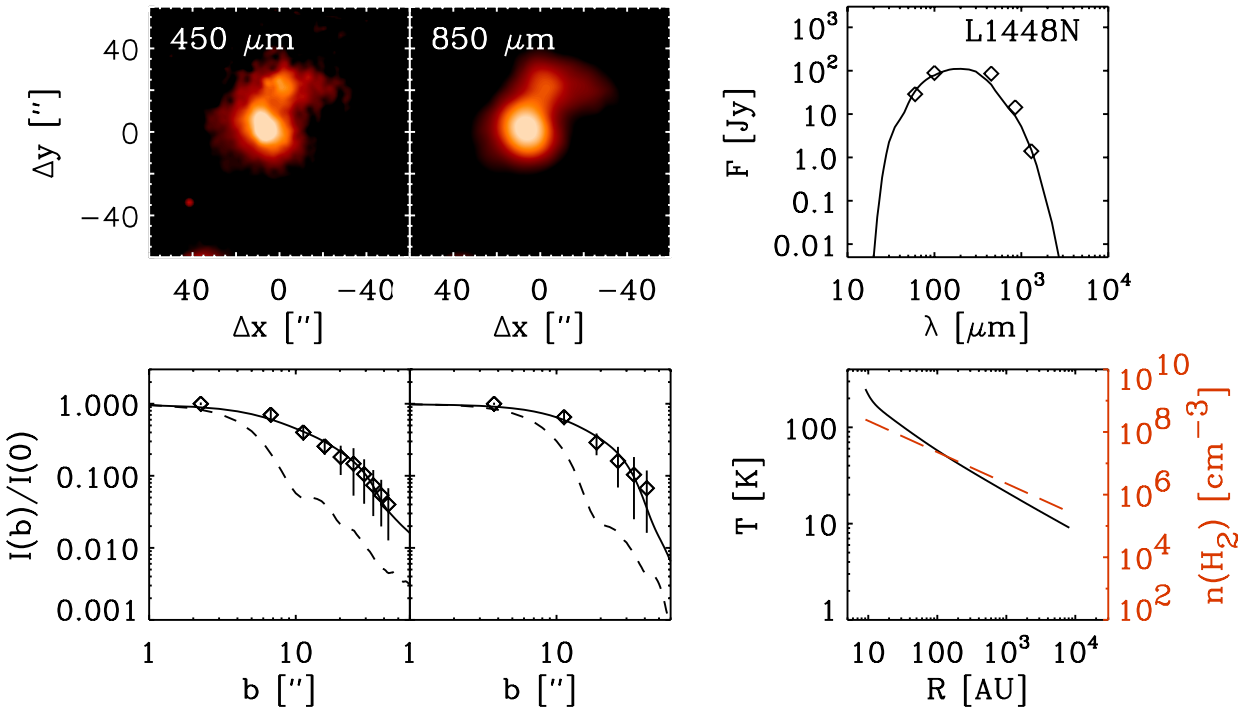


**Fig. A.1.** Observations and result of the modelling of L1448N. The upper left panel shows the SCUBA observations at 450 and 850 $\mu$m. The upper right panel shows the SED (diamonds) and the fitted model (solid line). The lower left panel shows the brightness profile and the fitted model. The dashed line represents the beam profile. The lower right panel shows the derived temperature dust (solid line) and density profile (dashed line).

**Table B.1.** Predicted line fluxes of selected o-$H_2CO$ transitions for a constant abundance $X_{out}$ across the enveloppe.

| Transition | Freq. (GHz) | $E_{up}$ ($cm^{-1}$) | Fluxes ($erg\,s^{-1}\,cm^{-2}$) | | | | | | | |
|---|---|---|---|---|---|---|---|---|---|---|
| | | | IRAS 4A | IRAS 4B | IRAS 2 | L1448MM | L1448N | L1157MM | L1527 | VLA1623 |
| $2_{1,2} - 1_{1,1}$ | 140.8 | 15 | 2.6E-15 | 1.6E-15 | 4.6E-16 | 1.1E-15 | 2.1E-15 | 3.7E-16 | 7.6E-16 | 3.8E-16 |
| $2_{1,1} - 1_{1,0}$ | 150.4 | 16 | 2.5E-15 | 1.4E-15 | 3.9E-16 | 9.2E-16 | 2.1E-15 | 3.5E-16 | 6.4E-16 | 3.6E-16 |
| $3_{1,3} - 2_{1,2}$ | 211.2 | 22 | 3.4E-15 | 1.6E-15 | 6.3E-16 | 1.1E-15 | 3.3E-15 | 5.6E-16 | 5.7E-16 | 4.3E-16 |
| $3_{1,2} - 2_{1,1}$ | 225.6 | 23 | 2.8E-15 | 1.1E-15 | 4.6E-16 | 6.5E-16 | 2.4E-15 | 4.4E-16 | 2.6E-16 | 3.2E-16 |
| $4_{1,4} - 3_{1,3}$ | 281.5 | 32 | 3.3E-15 | 1.1E-15 | 6.6E-16 | 7.5E-16 | 2.1E-15 | 5.3E-16 | 2.0E-16 | 3.2E-16 |
| $4_{3,2} - 3_{3,1}$ | 291.3 | 98 | 3.0E-17 | 3.3E-18 | 9.7E-18 | 4.6E-18 | 2.8E-18 | 3.7E-18 | 3.1E-19 | 1.5E-18 |
| $4_{3,1} - 3_{3,0}$ | 291.3 | 98 | 3.0E-17 | 3.3E-18 | 9.7E-18 | 4.6E-18 | 2.8E-18 | 3.7E-18 | 2.9E-19 | 1.5E-18 |
| $4_{1,3} - 3_{1,2}$ | 300.8 | 33 | 2.6E-15 | 5.8E-16 | 4.8E-16 | 4.1E-16 | 1.1E-15 | 3.9E-16 | 5.6E-17 | 2.1E-16 |
| $5_{1,5} - 4_{1,4}$ | 351.7 | 43 | 2.7E-15 | 5.3E-16 | 6.0E-16 | 4.4E-16 | 8.1E-16 | 4.0E-16 | 4.9E-17 | 2.0E-16 |
| $5_{3,3} - 4_{3,2}$ | 364.2 | 110 | 8.6E-17 | 7.1E-18 | 2.6E-17 | 9.5E-18 | 5.1E-18 | 1.0E-17 | 2.9E-19 | 3.7E-18 |
| $5_{3,2} - 4_{3,2}$ | 364.2 | 110 | 8.6E-17 | 7.1E-18 | 2.6E-17 | 9.5E-18 | 5.1E-18 | 1.0E-17 | 2.7E-19 | 3.7E-18 |
| $5_{1,4} - 4_{1,3}$ | 375.8 | 46 | 2.5E-15 | 3.8E-16 | 5.2E-16 | 3.0E-16 | 5.0E-16 | 3.6E-16 | 1.6E-17 | 1.6E-16 |
| $6_{1,6} - 5_{1,5}$ | 421.9 | 57 | 2.3E-15 | 3.1E-16 | 5.6E-16 | 2.9E-16 | 3.4E-16 | 3.2E-16 | 1.4E-17 | 1.4E-16 |
| $6_{3,4} - 5_{3,3}$ | 437.1 | 125 | 1.6E-16 | 1.0E-17 | 4.7E-17 | 1.4E-17 | 6.4E-18 | 1.8E-17 | 2.2E-19 | 5.9E-18 |
| $6_{3,3} - 5_{3,2}$ | 437.2 | 125 | 1.6E-16 | 1.0E-17 | 4.7E-17 | 1.4E-17 | 6.4E-18 | 1.8E-17 | 2.0E-19 | 6.0E-18 |
| $6_{1,5} - 5_{1,4}$ | 450.8 | 61 | 2.3E-15 | 2.3E-16 | 5.1E-16 | 2.1E-16 | 2.2E-16 | 3.0E-16 | 3.9E-18 | 1.2E-16 |
| $7_{1,7} - 6_{1,6}$ | 491.9 | 74 | 2.0E-15 | 1.9E-16 | 5.1E-16 | 1.9E-16 | 1.6E-16 | 2.7E-16 | 3.9E-18 | 1.0E-16 |
| $7_{3,5} - 6_{3,4}$ | 510.1 | 142 | 2.5E-16 | 1.2E-17 | 6.8E-17 | 1.7E-17 | 6.6E-18 | 2.7E-17 | 1.4E-19 | 7.7E-18 |
| $7_{3,4} - 6_{3,3}$ | 510.2 | 142 | 2.5E-16 | 1.2E-17 | 6.8E-17 | 1.7E-17 | 6.6E-18 | 2.7E-17 | 1.3E-19 | 7.7E-18 |
| $7_{1,6} - 6_{1,5}$ | 525.6 | 78 | 2.0E-15 | 1.5E-16 | 4.9E-16 | 1.6E-16 | 1.1E-16 | 2.6E-16 | 1.2E-18 | 9.0E-17 |
| $8_{1,8} - 7_{1,7}$ | 561.8 | 93 | 1.8E-15 | 1.2E-16 | 4.7E-16 | 1.4E-16 | 8.0E-17 | 2.2E-16 | 1.2E-18 | 7.4E-17 |
| $8_{3,6} - 7_{3,5}$ | 583.1 | 161 | 3.4E-16 | 1.3E-17 | 9.1E-17 | 1.9E-17 | 6.2E-18 | 3.6E-17 | 8.2E-20 | 8.9E-18 |
| $8_{3,5} - 7_{3,4}$ | 583.2 | 161 | 3.4E-16 | 1.3E-17 | 9.0E-17 | 1.8E-17 | 6.2E-18 | 3.6E-17 | 7.6E-20 | 8.8E-18 |
| $8_{1,7} - 7_{1,6}$ | 600.3 | 68 | 1.9E-15 | 1.1E-16 | 4.7E-16 | 1.2E-16 | 6.1E-17 | 2.3E-16 | 4.3E-19 | 6.9E-17 |
| $9_{1,9} - 8_{1,8}$ | 631.6 | 114 | 1.7E-15 | 8.7E-17 | 4.4E-16 | 1.1E-16 | 4.7E-17 | 2.0E-16 | 4.4E-19 | 5.8E-17 |
| $9_{3,7} - 8_{3,6}$ | 656.1 | 183 | 4.4E-16 | 1.4E-17 | 1.1E-16 | 1.9E-17 | 5.5E-18 | 4.5E-17 | 4.4E-20 | 9.5E-18 |
| $9_{3,6} - 8_{3,5}$ | 656.4 | 183 | 4.4E-16 | 1.4E-17 | 1.1E-16 | 1.9E-17 | 5.5E-18 | 4.4E-17 | 4.1E-20 | 9.5E-18 |
| $9_{1,8} - 8_{1,7}$ | 674.7 | 121 | 8.0E-17 | 1.8E-15 | 4.6E-16 | 9.8E-17 | 3.9E-17 | 2.1E-16 | 1.8E-19 | 5.6E-17 |
| $10_{1,10} - 9_{1,9}$ | 701.3 | 137 | 6.5E-17 | 1.7E-15 | 4.2E-16 | 8.3E-17 | 2.9E-17 | 1.9E-16 | 1.7E-19 | 4.6E-17 |
| $10_{3,8} - 9_{3,7}$ | 729.1 | 207 | 1.3E-17 | 5.3E-16 | 1.3E-16 | 1.8E-17 | 4.3E-18 | 5.1E-17 | 1.9E-20 | 9.2E-18 |
| $10_{1,9} - 9_{1,8}$ | 729.6 | 207 | 1.3E-17 | 5.2E-16 | 1.3E-16 | 1.8E-17 | 4.3E-18 | 5.1E-17 | 1.8E-20 | 9.2E-18 |
| $11_{1,11} - 10_{1,10}$ | 749.0 | 146 | 6.2E-17 | 1.8E-15 | 4.4E-16 | 7.9E-17 | 2.5E-17 | 1.9E-16 | 7.7E-20 | 4.5E-17 |
| $11_{1,10} - 10_{1,10}$ | 770.8 | 163 | 5.0E-17 | 1.7E-15 | 4.0E-16 | 6.5E-17 | 1.9E-17 | 1.7E-16 | 6.7E-20 | 3.7E-17 |
| $11_{1,10} - 10_{1,9}$ | 823.0 | 173 | 4.9E-17 | 1.8E-15 | 4.3E-16 | 6.5E-17 | 1.7E-17 | 1.9E-16 | 3.4E-20 | 3.7E-17 |
| $12_{1,12} - 11_{1,11}$ | 840.2 | 191 | 3.6E-17 | 1.6E-15 | 3.7E-16 | 4.8E-17 | 1.1E-17 | 1.6E-16 | 2.2E-20 | 2.8E-17 |
| $12_{1,11} - 11_{1,10}$ | 896.7 | 203 | 3.6E-17 | 1.8E-15 | 3.9E-16 | 4.8E-17 | 1.0E-17 | 1.7E-16 | 1.3E-20 | 2.8E-17 |

**Table B.2.** Predicted line fluxes of selected o-$H_2CO$ transitions for an abundance $X_{out}$ in the outer enveloppe, increasing to $X_{in}$ at the radius where $T_{dust} \geq 100$ K.

| Transition | Freq. | $E_{up}$ | Fluxes | | | | | | |
|---|---|---|---|---|---|---|---|---|---|
| | (GHz) | ($cm^{-1}$) | ($erg\,s^{-1}\,cm^{-2}$) | | | | | | |
| | | | IRAS 4A | IRAS 4B | IRAS 2 | L1448MM | L1448N | L1157MM | L1527 |
| $2_{1,2} - 1_{1,1}$ | 140.8 | 15 | 2.7E-15 | 1.6E-15 | 4.9E-16 | 1.1E-15 | 2.1E-15 | 3.7E-16 | 7.6E-16 |
| $2_{1,1} - 1_{1,0}$ | 150.4 | 16 | 2.5E-15 | 1.4E-15 | 4.2E-16 | 9.2E-16 | 2.1E-15 | 3.6E-16 | 6.4E-16 |
| $3_{1,3} - 2_{1,2}$ | 211.2 | 22 | 3.5E-15 | 1.7E-15 | 7.3E-16 | 1.1E-15 | 3.3E-15 | 5.9E-16 | 5.7E-16 |
| $3_{1,2} - 2_{1,1}$ | 225.6 | 23 | 2.9E-15 | 1.1E-15 | 5.8E-16 | 6.9E-16 | 2.4E-15 | 4.8E-16 | 2.7E-16 |
| $4_{1,4} - 3_{1,3}$ | 281.5 | 32 | 3.5E-15 | 1.1E-15 | 8.9E-16 | 8.1E-16 | 2.2E-15 | 6.2E-16 | 2.1E-16 |
| $4_{3,2} - 3_{3,1}$ | 291.3 | 98 | 1.6E-16 | 9.7E-17 | 2.8E-16 | 6.4E-17 | 4.6E-17 | 4.5E-17 | 9.2E-19 |
| $4_{3,1} - 3_{3,0}$ | 291.3 | 98 | 1.6E-16 | 9.6E-17 | 2.8E-16 | 6.4E-17 | 4.6E-17 | 4.5E-17 | 9.0E-19 |
| $4_{1,3} - 3_{1,2}$ | 300.8 | 33 | 2.9E-15 | 6.8E-16 | 7.7E-16 | 4.9E-16 | 1.1E-15 | 5.1E-16 | 6.0E-17 |
| $5_{1,5} - 4_{1,4}$ | 351.7 | 43 | 3.1E-15 | 6.9E-16 | 1.0E-15 | 5.6E-16 | 9.2E-16 | 6.2E-16 | 5.7E-17 |
| $5_{3,3} - 4_{3,2}$ | 364.2 | 110 | 4.6E-16 | 1.9E-16 | 5.6E-16 | 1.5E-16 | 1.1E-16 | 1.5E-16 | 2.3E-18 |
| $5_{3,2} - 4_{3,2}$ | 364.2 | 110 | 4.6E-16 | 1.9E-16 | 5.6E-16 | 1.5E-16 | 1.2E-16 | 1.5E-16 | 2.3E-18 |
| $5_{1,4} - 4_{1,3}$ | 375.8 | 46 | 3.0E-15 | 5.7E-16 | 1.1E-15 | 4.5E-16 | 6.4E-16 | 6.2E-16 | 2.5E-17 |
| $6_{1,6} - 5_{1,5}$ | 421.9 | 57 | 3.0E-15 | 5.7E-16 | 1.3E-15 | 4.9E-16 | 5.4E-16 | 7.2E-16 | 2.7E-17 |
| $6_{3,4} - 5_{3,3}$ | 437.1 | 125 | 9.2E-16 | 3.2E-16 | 9.6E-16 | 2.6E-16 | 2.1E-16 | 3.2E-16 | 3.9E-18 |
| $6_{3,3} - 5_{3,2}$ | 437.2 | 125 | 9.2E-16 | 3.2E-16 | 9.6E-16 | 2.6E-16 | 2.2E-16 | 3.2E-16 | 4.0E-18 |
| $6_{1,5} - 5_{1,4}$ | 450.8 | 61 | 3.1E-15 | 5.5E-16 | 1.4E-15 | 4.7E-16 | 4.6E-16 | 7.9E-16 | 1.7E-17 |
| $7_{1,7} - 6_{1,6}$ | 491.9 | 74 | 3.1E-15 | 6.0E-16 | 1.7E-15 | 5.2E-16 | 4.6E-16 | 9.2E-16 | 2.0E-17 |
| $7_{3,5} - 6_{3,4}$ | 510.1 | 142 | 1.5E-15 | 4.9E-16 | 1.5E-15 | 3.9E-16 | 3.4E-16 | 5.7E-16 | 4.8E-18 |
| $7_{3,4} - 6_{3,3}$ | 510.2 | 142 | 1.5E-15 | 4.9E-16 | 1.4E-15 | 3.9E-16 | 3.4E-16 | 5.6E-16 | 4.9E-18 |
| $7_{1,6} - 6_{1,5}$ | 525.6 | 78 | 3.4E-15 | 6.6E-16 | 1.9E-15 | 5.6E-16 | 4.8E-16 | 1.1E-15 | 1.7E-17 |
| $8_{1,8} - 7_{1,7}$ | 561.8 | 93 | 3.4E-15 | 7.5E-16 | 2.2E-15 | 6.3E-16 | 5.4E-16 | 1.2E-15 | 1.8E-17 |
| $8_{3,6} - 7_{3,5}$ | 583.1 | 161 | 2.3E-15 | 7.4E-16 | 2.2E-15 | 5.9E-16 | 5.2E-16 | 9.1E-16 | 4.9E-18 |
| $8_{3,5} - 7_{3,4}$ | 583.2 | 161 | 2.3E-15 | 7.4E-16 | 2.2E-15 | 5.9E-16 | 5.2E-16 | 9.1E-16 | 5.0E-18 |
| $8_{1,7} - 7_{1,6}$ | 600.3 | 68 | 3.9E-15 | 8.6E-16 | 2.6E-15 | 7.2E-16 | 6.2E-16 | 1.5E-15 | 1.5E-17 |
| $9_{1,9} - 8_{1,8}$ | 631.6 | 114 | 4.1E-15 | 1.0E-15 | 3.0E-15 | 8.3E-16 | 7.2E-16 | 1.7E-15 | 1.5E-17 |
| $9_{3,7} - 8_{3,6}$ | 656.1 | 183 | 3.2E-15 | 1.0E-15 | 3.1E-15 | 8.3E-16 | 7.3E-16 | 1.3E-15 | 3.9E-18 |
| $9_{3,6} - 8_{3,5}$ | 656.4 | 183 | 3.2E-15 | 1.0E-15 | 3.1E-15 | 8.3E-16 | 7.3E-16 | 1.3E-15 | 4.0E-18 |
| $9_{1,8} - 8_{1,7}$ | 674.7 | 121 | 4.7E-15 | 1.2E-15 | 3.6E-15 | 9.6E-16 | 8.5E-16 | 2.0E-15 | 1.3E-17 |
| $10_{1,10} - 9_{1,9}$ | 701.3 | 137 | 5.1E-15 | 1.4E-15 | 4.1E-15 | 1.1E-15 | 9.8E-16 | 2.3E-15 | 1.0E-17 |
| $10_{3,8} - 9_{3,7}$ | 729.1 | 207 | 4.2E-15 | 1.4E-15 | 4.1E-15 | 1.1E-15 | 9.2E-16 | 1.8E-15 | 2.2E-18 |
| $10_{1,9} - 9_{1,8}$ | 729.6 | 207 | 4.1E-15 | 1.4E-15 | 4.1E-15 | 1.1E-15 | 9.1E-16 | 1.8E-15 | 2.2E-18 |
| $11_{1,11} - 10_{1,10}$ | 749.0 | 146 | 5.8E-15 | 1.6E-15 | 4.8E-15 | 1.3E-15 | 1.1E-15 | 2.7E-15 | 8.5E-18 |
| $11_{1,10} - 10_{1,10}$ | 770.8 | 163 | 6.3E-15 | 1.8E-15 | 5.4E-15 | 1.4E-15 | 1.3E-15 | 3.0E-15 | 6.4E-18 |
| $11_{1,10} - 10_{1,9}$ | 823.0 | 173 | 7.3E-15 | 2.1E-15 | 6.3E-15 | 1.7E-15 | 1.5E-15 | 3.5E-15 | 5.1E-18 |
| $12_{1,12} - 11_{1,11}$ | 840.2 | 191 | 7.9E-15 | 2.4E-15 | 7.0E-15 | 1.8E-15 | 1.6E-15 | 3.7E-15 | 2.9E-18 |
| $12_{1,11} - 11_{1,10}$ | 896.7 | 203 | 9.1E-15 | 2.8E-15 | 8.2E-15 | 2.1E-15 | 1.8E-15 | 4.3E-15 | 2.4E-18 |